UNIVERSITY OF TWENTE.

2D Box Traps for Bose-Einstein Condensates

Maarten T.M. Christenhusz
B.Sc

Under the supervision of
Dr. Tyler W. Neely &
Prof. Pepijn W.H. Pinkse

A thesis submitted to the University of Twente
in partial fulfilment of the degree of Master of Science
Faculty of Science and Technology
February 2020

Typeset in $\LaTeX\,2_\varepsilon$.

The work presented in this Thesis is, to the best of my knowledge and belief original, except as acknowledged in the text, and has not been submitted either in whole or in part, for a degree at this or any other university.

Maarten T.M. Christenhusz

Abstract

Optical dipole traps (ODTs) are among the most commonly used traps for confining Bose-Einstein condensates (BECs). A high degree of control of light allows for the realisation of a great variety of trapping geometries. One of the simplest, yet elegant methods of trapping BECs is in an ODT is using a focussed red-detuned laser beam, which acts as an attractive potential. While such a trap is easily realised and is very robust, it nevertheless poses various disadvantages. To achieve a high degree of vertical atom confinement, i.e. a large trap frequency, the trap area and uniformity have to be sacrificed due to the Gaussian nature of the beam. In addition, when combining these traps with structured repulsive potentials, atoms which are not part of the condensate (thermal atoms) may float outside of the structures while still attracted to the red-detuned ODT. This results in noise in measurements and prevents various experiments from being conducted.

In this thesis, a new trap is proposed which overcomes these issues. Through combining two blue-detuned beams, which act as a repulsive potential, an optical lattice is formed. Atoms are vertically confined in at the nodal planes and horizontally using another blue-detuned beam. This allows for creation of nearly uniform traps, closely resembling a finite-potential square well. The lattice spacing is easily adjusted, which provides stronger vertical confinement, making the trap a 2D box trap for BECs.

We propose and realise the implementation of such a 2D box trap. After characterization, a BEC lifetime in the trap of 19(5) s was found, which, while lower than the current red-sheet beam trap, is a sufficient lifetime for 2D transport and turbulence experiments. A trap frequency of $\nu_{\text{trap}} = 58(1)$ Hz was realised at low trap powers and at a large lattice spacing. By increasing the beam power and reducing the lattice spacing, a theoretical maximum of over 10 kHz can be achieved.

While future work on the trap will have to experimentally demonstrate these higher trap frequencies, the trap lifetime and uniformity have already opened possibilities to new experiments, such as the experimental identification of a superfluid Reynolds number. Other future experiments made possible by the higher trap depth and frequency include observation of the superfluid fountain effect and observation of quantized conductance for bosons.

Acknowledgements

This thesis is the result of what I explained to my friends as many hours of aligning optics. However at times it felt like that, this does not encompass all of the amazing and fascinating things I got to do at (and outside of) UQ. As such, even though it is not very common to write an acknowledgement for a master thesis in my university, I still felt it more than appropriately to do so. If anything, I don't think I have to worry too much about what is and isn't regular at my university, being "one of a handful" of Applied Physics students who not only decided to not do their master project outside the research groups within the university, but almost literally on the other side of the world.

First and foremost, I would like to thank Dr. Tyler Neely, my main supervisor for all his help, guidance and patience during the project. Thank you for your enthusiasm on our first video call in which you told me about what you were currently up to in the lab and the proposals for research projects you gave me then. I don't think anyone was really expecting setting up a setup for "some improved optical trapping" which "only needed to be put on the table" would turn out to be such a challenging, but because of that, rewarding experience. Even though not being new to experimental projects, I don't think I've ever felt more like an experimental physicist than in the lab here. At times, my mind was blown when troubleshooting while I was trying to figure out what was going on, and you had already found out what was wrong and what electric circuit we needed to build to fix it. Thank you for always making time to help when I needed it and for your support throughout the 10 months in which I had the amazing opportunity to work on your experiment.

I'd like to thank my secondary supervisor, Prof. Pepijn Pinkse for his help and advice from afar. I'd like to thank Jan Klärs for writing an excellent reference for me that got me to do my project at UQ and I'd like to thank Prof. Matt Davis for helping me get in touch with Tyler.

My project would not have turned out like it has without my colleagues, least of all Guillaume Gauthier. Thank you for the endless amounts of times you helped me in setting up the Green Sheet, whenever I would not understand something, or whenever I just needed someone to help me stay sane sometimes. Not only were you a great lab partner, you were also an excellent gym buddy and fellow band member of the infamous French Kiss. Thank you to Kwan for showing me the ropes of the experiment when I was just a lab-rookie and thank you Callam for helping me set-up the Green Sheet and for your great song covers while we were experimenting. I'd also like to thank Alex, Tom and Mark for the interesting discussions and patience whenever I would 'borrow' some optics from your new setup. You've all been great friends to me during my time Down Under.

Thank you to all my friends outside of UQ for experiencing and exploring Australia with me, and for sticking with me through the good times and the bad. It is a wonderful feeling to know there is always someone to talk to and hang out with whenever all your friends and family on the other side of the world are fast asleep. Thank you, Sarah, Kate, Steve, Nathalie and all the others for exploring all the wonderful and weird places in Australia and Brisbane with me.

Last but not least I'd like to thank my family and friends for all your support from the other side of the world. It must not have been easy for you, mom, dad and Femke to hear me say "I think I would like to go abroad for a while again, but this time not for four but ten months, and on the other side of the world" and even though I could never quite explain what it was I was doing and why I couldn't do it close to home, I would still like to thank you for all your support.

Contents

Abstract **v**

Acknowledgements **vii**

List of Figures **xi**

List of Tables **xiii**

List of Acronyms & Symbols **xv**

1 Introduction **1**

2 Theoretical Background **3**
- 2.1 Bose-Einstein Condensation 4
  - 2.1.1 A collapse to the ground state 4
  - 2.1.2 Microscopic theory of BECs 5
  - 2.1.3 Superfluids 6
- 2.2 Trapping and cooling of atoms 8
  - 2.2.1 Hyperfine structure of atoms 8
  - 2.2.2 Optical dipole trapping 9

3 A Versatile BEC Apparatus **13**
- 3.1 Creation of Bose-Einstein condensates 13
- 3.2 Configuring BECs with Digital Micromirror Devices 16
- 3.3 Imaging techniques for Bose-Einstein Condensates 17

4 Experimental Design **19**
- 4.1 Trapping atoms in a blue-detuned optical lattice 20
- 4.2 Experimental Setup Summary 21
  - 4.2.1 Bottom optical table 21
  - 4.2.2 The tower 22
  - 4.2.3 Top optical table 23
- 4.3 Phase locking using active feedback 24
- 4.4 Polarisation-maintaining fibres 27
- 4.5 Conclusion 29

5 Characterization of the optical lattice **31**
5.1 The lifetime of anti-harmonically trapped BECs . . . 32
5.1.1 Background . . . 32
5.1.2 Experimental sequence . . . 33
5.1.3 Results and discussion . . . 33
5.2 Trap frequency of the optical lattice . . . 35
5.2.1 Background . . . 35
5.2.2 Modelling the optical lattice . . . 36
5.2.3 Experimental Sequence . . . 36
5.2.4 Results and discussion . . . 37

6 Applications **41**
6.1 Superfluid analogue to the Reynolds number . . . 42
6.1.1 Introduction . . . 42
6.1.2 Previous experimental studies . . . 43
6.1.3 Proposed experiment . . . 44
6.2 Superfluid fountain effect . . . 45
6.2.1 Introduction . . . 45
6.2.2 Previous experimental studies . . . 47
6.2.3 Proposed experiment . . . 48
6.3 Quantized conductance of bosons . . . 49
6.3.1 Introduction . . . 49
6.3.2 Previous and proposed experimental studies . . . 49

7 Conclusion **51**

A A detailed look at the optical lattice setup **53**
A.1 A walk-through of all components . . . 53
A.2 Thermal lensing in AOMs . . . 57
A.2.1 Introduction . . . 57
A.2.2 Background . . . 58
A.2.3 Experimental implementation . . . 59

References **63**

List of Figures

3.1 The vacuum system of the UQ BEC Experiment 14
3.2 The hyperfine structure of ^{87}Rb 15
3.3 Imprinted patterns in a BEC using DMDs 17

4.1 Optical setup for creating two identical beams for an optical lattice 21
4.2 Bottom optical table setup 22
4.3 Top optical table setup 23
4.4 Shaking of the lattice due to phase noise 24
4.5 In and out of phase lattice 25
4.6 Illustration of setting the relative phase difference and locking the system . . 26
4.7 Trap depth with unbalanced beam powers 27
4.8 Power drift in the beams over time when aligning the optical fibre 30

5.1 Lifetime measurement experimental sequence 33
5.2 Lifetime Experimental Data Plot 34
5.3 Simulated trap depth and frequency 36
5.4 Trap frequency measurement experimental sequence 37
5.5 Trap Frequency Experimental Data Plot 37
5.6 The optical lattice with atom loaded in trap in situ 39

6.1 Density images of atoms loaded into the optical lattice and the red sheet trap 43
6.2 Numerical data to the superfluid Reynolds number 44
6.3 The three different regimes in the von Kármán vortex street 45
6.4 Superfluid fountain effect in Helium-II 46
6.5 Experimental sequence of a previous experimental study at UQ to the fountain effect 47

A.1 Bottom optical table setup – extended 54
A.2 Top optical table setup – extended 56
A.3 Setup for measuring thermal lensing 59
A.4 The measured thermal lensing 60

List of Tables

4.1 Extinction ratio data for the polarisation maintaining fibre 28

List of Acronyms & Symbols

Throughout the thesis, many acronyms and symbols are used. The following list is neither exhaustive nor exclusive, but may be helpful.

List of Acronyms

2D . . . . Two-dimensional

AOM . . . . Acousto-optic modulator

BEC . . . . Bose-Einstein condensate

DMD . . . . Digital micromirror device

GPE . . . . Gross-Pitaevskii equation

MOT . . . . Magneto-optical trap

MW . . . . Microwave

ODT . . . . Optical dipole trap

PBS . . . . Polarizing beamsplitter

PI-controller . . . Proportional Integral controller

PMF . . . . Polarization-maintaining fibre

Rb . . . . Rubidium

TOF . . . . Time of flight

List of Symbols

$\hat{H}$ . . . . Hamiltonian

$\lambda_{\mathrm{lattice}}$ . . . . The fringe spacing of the optical lattice

μ . . . . Chemical potential

ν . . . . Trap frequency

ξ . . . . Healing length

τ . . . . Lifetime

$\hat{\Psi}^\dagger$, $\hat{\Psi}$ . . . . Bosonic creation and annihilation operators

ψ . . . . Mean-field wavefunction

1 Introduction

Bose-Einstein condensation was first achieved in 1995 by Cornell and Wieman's group using Rubidium atoms [1] and later in the same year by Ketterle's group at MIT using Sodium atoms [2]. Ever since, many Bose-Einstein condensate (BEC) experiments have been realised, counting more than 250 experimental and theory groups in cold atoms around the world and even outside, with one BEC experiment aboard of the International Space Station. Ever since first realisation, cooling and trapping mechanisms for atoms have drastically improved. The ability to have very high resolution and dynamic control over atomic clouds, for example through use of a digital micromirror device (DMD) [3], have made BECs such a versatile medium in which to study a wide range of topics in physics, ranging from high precision metrology [4] to atomic analogues of electrical circuits [5, 6] to studies of turbulence [7].

Key to performing experiments on BECs is confinement atoms. The most common method of trapping atoms in a BEC is through the use of optical dipole traps (ODTs), in the dipole moment of an atom is exploited by exerting a force gradient on the atoms using an electric field. When studying the topic of two-dimensional (2D) transport and turbulence, it is essential to be able to confine atoms strongly enough for the condensate to be considered 2D. At the University of Queensland (UQ), this is currently by focussing a red-detuned laser beam, which acts as an attractive potential, on the atom plane. While this is an elegant and simple method of trapping atoms, the current red-detuned ODT brings various disadvantages with it. Increasing the vertical confinement, required for various experiments, always sacrifices the area of the beam in which atoms are confined, due to the nature of Gaussian beam optics. Another disadvantage, unique to the current trap at UQ, is atoms that are still attracted to the red-detuned trap, but float outside the DMD-potential trap in which we conduct our experiments. These atoms, called thermal atoms, are not condensed and have a higher energy, and may therefore float outside of the DMD-potential trap. Thermal atoms introduce noise and disrupt experiments.

A new trap which overcomes these issues, inspired by Ville et al. [8] is implemented and demonstrated in the BEC experiment at UQ. Using two identical blue-detuned beams, which implements a repulsive potential, an ODT trap is realised, shaped through the interference of the two beams. The interference pattern forms an optical lattice, in which the atoms are trapped in the nodes. While the area of the trap is still determined by the (horizontal) Gaussian beam waist and the Rayleigh length, the vertical confinement (the trap frequency) is determined and can be controlled by changing the lattice spacing of the trap. This allows one to create harmonic traps which are nearly flat while having a high degree of control over the trap frequency. Furthermore, because of the repulsive nature of the trap, any thermal atoms are expelled outside of the DMD pattern.

In this thesis, the implementation and characterization of this optical lattice trap is presented. Chapter 2 is an introduction to anyone who is unfamiliar with BECs and describes the physics relevant to the work discussed in the thesis. In Chapter 3, the experimental apparatus at UQ is described. The vacuum system and the cooling and trapping mechanisms to achieve Bose-Einstein condensation are described in the first part. The second part describes the DMD trap, pioneered at UQ, which is used to dynamically control the condensate in the conducted experiments. The remainder of the Chapter describes techniques used to image BECs. In Chapter 4, the experimental design of the optical lattice is discussed. In the first part, the working principles behind the trap are explained, followed by the experimental setup. In the remainder of the Chapter, the necessity for using an active lattice stabilization feedback system and other important considerations to take into account are discussed. The optical lattice trap is characterized in Chapter 5. An experiment for measuring the lifetime of a BEC in the trap is discussed in Section 5.1, and in Section 5.2, the trap frequency at the moment of implementation of the trap is measured. Chapter 6 serves as an outlook and discusses three different experiments which can be conducted with the new trap, with each of these experiments utilizes a different new feature of the trap. Chapter 7 concludes the thesis by summarizing the thesis and giving a future outlook for the work.

2
Theoretical Background

Bose-Einstein condensation was first predicted by Albert Einstein. In a paper published in 1924-1925 [9], Einstein followed up on a paper written by Bose from 1924 [10]. Bose's paper described a quantum theory of photon statistics, based on Planck's famous radiation formula of the light quanta. Einstein expanded this idea to massive particles which resulted in the concept of a Bose gas, which follows the Bose-Einstein distribution. He proposed that cooling bosonic atoms to a temperature close to absolute zero would cause them to condense into the lowest accessible quantum state. It was not until 1995 that the first BEC was experimentally realised by Cornell and Wieman's group at the University of Colorado using Rubidium atoms [1] and not much later by Ketterle's group at MIT using Sodium atoms [2].

The timespan between the theoretical description of BECs and the first experimental realisation was long due to technical limitations. It was not until 1987 that laser Doppler cooling was first demonstrated [11], which allows ^{87}Rb to cool down to $T_{\mathrm{Doppler}} = 146\,\mu\mathrm{K}$ [12]. Additional cooling techniques, such as evaporative cooling [13], are however to be used in combination with laser Doppler cooling in order to get to the critical temperature needed for condensation.

In the first section of this chapter, a general theoretical description of BECs and quantum fluids is given. Before touching on a quantum description of Bose-Einstein condensation, bosonic properties and statistics which lead to this exotic state of matter are discussed. Based on the Hamiltonian for a system of interacting particles, a mean field description is given, which leads to the Schrödinger equation analogue for BECs, the Gross-Pitaevskii equation (GPE). The final part of the section is dedicated to what the GPE implies for the superfluid behaviour of BECs. Sections 2.2.1 and 2.2.2 discuss the atomic structure and how the atomic properties are exploited in cooling and trapping techniques to experimentally create BECs. In particular, Sec. 2.2.2 describes the physics behind the trapping mechanism used in the optical lattice trap presented in this thesis and presents the mathematics used to simulate ODTs, as is done later in Chapter 5.

2.1 Bose-Einstein Condensation

2.1.1 A collapse to the ground state

Any particle can be categorized as either a boson or fermion. Bosons and fermions behave fundamentally different from each other as result of a different spin: Any particle with a half-integer spin is classified as a fermion and any full-integer particle is classified as a boson. The difference in full or half-integer spin changes the symmetry properties of their wavefunction. While the wavefunction of bosons is invariant upon changing position of two particles, the wavefunction for a fermionic system changes sign upon particle position exchange [14]:

$$\Psi_{\text{boson}}(\mathbf{r}_1, \mathbf{r}_2) = \Psi_{\text{boson}}(\mathbf{r}_2, \mathbf{r}_1); \qquad \Psi_{\text{fermion}}(\mathbf{r}_1, \mathbf{r}_2) = -\Psi_{\text{fermion}}(\mathbf{r}_2, \mathbf{r}_1). \tag{2.1}$$

This fundamental symmetry property leads to the Pauli exclusion principle for fermions, but does not apply to bosons and, as such, allows different non-distinguishable bosons to occupy the same energy state simultaneously. Bose and Einstein realised that at sufficiently low temperatures, the probability of finding bosons in excited states decreases drastically. This leads to macroscopic occupation of the lowest energy state, the ground state. The occupation probability distribution of bosonic atoms is now commonly referred to as the Bose-Einstein distribution,

$$f_{\text{BE}} = \frac{1}{e^{(\epsilon-\mu)/k_B T} - 1}, \tag{2.2}$$

with ϵ and μ the energy and chemical potential of the atom, k_B Boltzman's constant and T the temperature.

The temperatures at which macroscopic occupation of the ground state occurs, referred to as the critical temperature are different depending on whether condensation occurs in free space or in a trap. The optical lattice trap realised in this thesis can be approximated as a harmonic trap. The critical temperature for non-interacting particles in a harmonic trap is given by

$$T_c = \frac{1}{k_B m} \left(\frac{\sqrt{2}\pi^2 \hbar^3 N}{V \Gamma\left(\frac{3}{2}\right) \zeta\left(\frac{3}{2}\right)} \right)^{3/2}, \tag{2.3}$$

in which N is the number of atoms, V the volume, m the atom mass, $\hbar$ the reduced Planck constant, and $\Gamma\left(\frac{3}{2}\right)$ and $\zeta\left(\frac{3}{2}\right)$ the gamma and Riemann zeta function for a non-interacting (free) gas [15].

Qualitatively, at this temperature the de Broglie wavelength, $\lambda = \sqrt{2\pi\hbar^2/(m\,k_B T)}$ [16], becomes of comparable length to the interatomic spacing. At this point the individual atoms become indistinguishable and can no longer be described by individual wavefuntions, but instead must be described as a macroscopic, coherent wavefunction.

2.1.2 Microscopic theory of BECs

Even though experimental BECs are considered dilute gases, densities are high enough to have inter-atomic collisions play a significant role. A complete description of atomic BECs would therefore be incomplete without including a two-body interaction term. In second quantization language, the Hamiltonian for a system of interacting particles is given by [17]

$$\hat{H} = \int d^3\mathbf{r}\,\hat{\Psi}^\dagger(\mathbf{r}) \left[-\frac{\hbar^2}{2m}\nabla^2 + V_{\text{ext}}(\mathbf{r}) + \frac{1}{2}\hat{\Psi}^\dagger(\mathbf{r}')V(\mathbf{r}-\mathbf{r}')\hat{\Psi}(\mathbf{r}') \right] \hat{\Psi}(\mathbf{r}), \tag{2.4}$$

in which $\hat{\Psi}^\dagger(\mathbf{r})$ and $\hat{\Psi}(\mathbf{r})$ are the bosonic creation and annihilation operators that create or remove a particle at $\mathbf{r}$, V_{ext} the external (applied) potential and $V(\mathbf{r}-\mathbf{r}')$ the two-body interaction potential.

BECs are sufficiently dilute to only consider s-wave collisions. This allows one to approximate the two-body interaction potential $V(\mathbf{r}-\mathbf{r}')$ to an effective pseudo-potential term $V(\mathbf{r}-\mathbf{r}') = g\delta(\mathbf{r}-\mathbf{r}')$, where the interaction term

$$g = \frac{4\pi\hbar^2 a_s}{m} \tag{2.5}$$

is characterized by the s-wave scattering length a_s. The delta function in the potential implies the interaction between the atoms is point-like.

To investigate quantum fluid flow and transport phenomena, it is useful to apply additional approximations, allowing to find an effective, mean-field wavefunction $\psi(\mathbf{r},t)$ for the bosonic field operator $\hat{\Psi}(\mathbf{r},t)$. To obtain this effective wavefunction, the Bologiubov approximation is made. This approximation decomposes the field operator $\hat{\Psi}(\mathbf{r},t)$ into an effective, condensate wavefunction, $\psi(\mathbf{r},t) = \left\langle \hat{\Psi}(\mathbf{r},t) \right\rangle$ and a term $\delta\hat{\Psi}(\mathbf{r},t)$, which accounts for all the remaining modes:

$$\hat{\Psi}(\mathbf{r},t) = \psi(\mathbf{r},t) + \delta\hat{\Psi}(\mathbf{r},t). \tag{2.6}$$

As the temperature $T \to 0$, all particles are in the ground state and the remaining modes $\delta\hat{\Psi}(\mathbf{r},t) \to 0$. Substituting the remaining mean-field wavefunction $\psi(\mathbf{r},t)$ and the Hamiltonian (Eq. 2.4) with pseudo-potential $V(\mathbf{r}-\mathbf{r}') = g\delta(\mathbf{r}-\mathbf{r}')$ into the Heisenberg equation,

$$i\hbar\frac{\partial\psi(\mathbf{r},t)}{\partial t} = \left[\psi(\mathbf{r},t), \hat{H}\right], \tag{2.7}$$

one obtains the Gross-Pitaevskii equation (GPE), which is widely used in simulating quantum fluid flows:

$$i\hbar\frac{\partial\psi(\mathbf{r},t)}{\partial t} = \left[-\frac{\hbar^2}{2m}\nabla^2 + V_{\text{ext}}(\mathbf{r}) + g\,|\psi(\mathbf{r},t)|^2\right]\psi(\mathbf{r},t). \tag{2.8}$$

The GPE closely resembles the time-dependent Schrödinger equation with an added non-linear term, $g\,|\psi(\mathbf{r},t)|^2$, to describe the inter-particle interactions. Furthermore, if V_{ext} is time-independent (as is often the case), Eq. 2.8 can be split using separation of variables (i.e. $\psi(\mathbf{r},t) = \psi(\mathbf{r})\phi(t)$), which gives a time-dependent and a time-independent solution. Solving for the spatial part gives

$$\left[-\frac{\hbar^2}{2m}\nabla^2 + V_{\text{ext}}(\mathbf{r}) + g\,|\psi(\mathbf{r})|^2\right]\psi(\mathbf{r}) = \mu\,\psi(\mathbf{r}), \tag{2.9}$$

which, consequently, closely resembles the time-independent Schrödinger equation. A notable difference is that for solving the eigenvalue, the chemical potential μ, the energy which is required to add another particle to the system, is found instead of the energy ϵ of an eigenstate.

In large systems, the kinetic energy is often negligible compared to the inter-particle interactions. In these systems an analytical solution can be found for the chemical potential μ by utilizing the Thomas-Fermi approximation. When neglecting the kinetic energy, the GPE (Eq. 2.9) becomes

$$\left[V(\mathbf{r}) + g\,|\psi(\mathbf{r})|^2\right]\psi(\mathbf{r}) = \mu\,\psi(\mathbf{r}), \tag{2.10}$$

which has the solutions

$$|\psi(\mathbf{r})|^2 = \begin{cases} \dfrac{\mu - V(\mathbf{r})}{g} & \text{for}\,\mu \geq V(\mathbf{r}) \\ 0 & \text{otherwise,} \end{cases} \tag{2.11}$$

where $\int \mathrm{d}^3\mathbf{r}\,|\psi(\mathbf{r})|^2 = \mathrm{N}$ is the number of atoms in the condensate.

The Thomas-Fermi approximation is particularly useful to find the ground state energy or the number of atoms, given the chemical potential, in the bulk BEC. It fails near the edge of the condensate, at which the kinetic energy is sufficiently high. In Chapter 3, the Thomas-Fermi approximation is used in the binodal fitting used to obtain the number of atoms in the BEC and the thermal cloud.

2.1.3 Superfluids

Upon achieving Bose-Einstein condensation, several length scales and other characteristic properties become relevant in order to understand and successfully execute simulations and experiments in the superfluid BEC. Along with the scattering length, a_s, which along with the mass determines in the interaction term in the GPE, another relevant length scale in superfluids is the coherence or healing length, ξ. This is the distance over which the BEC goes from zero back to its bulk density, n_0, in response to a local perturbation.

The healing length can be found by considering the GPE (Eq. 2.8) in 1D without external potential with the boundary conditions $\psi(0) = 0$ and $\lim_{x\to\infty} \psi(x) = \psi_0$ with $|\psi_0|^2 = n_0$. These boundary conditions imply the probability of finding the BEC on the edge and outside the condensate, or on some local perturbation, is 0 ($n = |\psi(x)|^2$) and far from the edge density is at its bulk value. This gives the analytic solution

$$\psi(x) = \psi_0 \tanh\left(\frac{\sqrt{mn_0 g}}{\hbar} x\right) = \sqrt{n_0} \tanh\left(\frac{x}{\xi}\right), \tag{2.12}$$

with $\xi = \hbar/\sqrt{mn_0 g}$ the healing length.

Much like other condensed matter systems, excitations are carried by phonons. These Bogoliubov excitations travel at the speed of sound in the system, $c = \sqrt{\mu/m}$, much like sound travels through air. The speed of sound can be used to measure the chemical potential and is of relevance in the experiments described in Chapter 6.

It is useful to express the wavefunction obtained from the GPE in terms of a density and a phase. To get the wavefunction in the polar representation, the Madelung transformation is applied. The wavefunction then becomes

$$\psi(\mathbf{r}, t) = \sqrt{n(\mathbf{r}, t)} \exp\left(i\phi(\mathbf{r}, t)\right), \tag{2.13}$$

with $n(\mathbf{r}, t)$ and $\phi(\mathbf{r}, t)$ the density and the phase of the condensate. The velocity field at time t is given by

$$\mathbf{v}(\mathbf{r}, t) = \frac{\hbar}{m} \nabla\phi(\mathbf{r}, t). \tag{2.14}$$

The vorticity of the quantum fluid, which is given by taking the curl of the velocity field, must be zero because of the vector calculus identity $\nabla \times \nabla\phi(\mathbf{r}, t) = 0$. This leads to an irrotational velocity field for quantum fluids. Circulation therefore requires a discontinuity in the phase manifested as a pole. The wavefunction is still required to be single-valued around the pole. The circulation is found using the well-known theorem from complex function theory, Cauchy's residue theorem,

$$\Gamma = \oint \mathrm{d}\mathbf{r}\, \mathbf{v}(\mathbf{r}, t) = \frac{\hbar}{m} \oint \mathrm{d}l\, \nabla\phi(\mathbf{r}, t) = \frac{\hbar}{m} 2\pi n = \frac{h}{m} n = \kappa n, \tag{2.15}$$

with $n \in \mathbb{Z}$. This means vortices in a BEC are quantised in units of $\kappa = h/m$. The value n determines the winding number, called charge, of the vortex. The charge is given by the number of times the phase goes through a 2π winding, which generally is ± 1, clockwise or counter-clockwise. Higher charge vortices require more energy and generally decay into multiple single charge vortices, in which the charge a conserved quantity.

Quantized vortices appear in all superfluids and their presence leads to many interesting physical phenomena such as the presence of turbulence in superfluids. Although inviscid, the presence of turbulence can be observed from vortex shedding by a cylindrical obstacle. Through a study of the dynamical similarities of shedding on a classical and superfluid, a Reynolds number for superfluids can be found. Chapter 6 discusses an experiment in which quantized vortices are used to experimentally observe the superfluid Reynolds number, based on a numerical study [18].

2.2 Trapping and cooling of atoms

2.2.1 Hyperfine structure of atoms

While nearly all atoms have bosonic isotopes, not all atoms are suitable for Bose-Einstein condensation. Many elements have electronic transitions that cannot be used with laser cooling, which reduces the number of available BEC candidates. ^{23}Na, ^{87}Rb, ^{39,41}K, ^{7}Li, ^{1}H, ^{4}He, ^{133}Cs, ^{52}Cr, ^{84}Sr, ^{170,174}Yt, ^{40}Ca, ^{164}Dy and ^{168}Er are all atoms in which Bose-Einstein condensation has been achieved to date. Many of these are of the alkali-atom group. Their electronic structure makes them excellent candidates for trapping and cooling.

All alkali atoms consist of fully filled electrons shells except for the outer shell, which is filled by a single electron and hence is in s-orbital. Because the electrons have no angular momentum, there is no fine splitting and the only coupling between the nucleus and electrons is due to the hyperfine interaction. The hyperfine splitting is a consequence of the magnetic field produced by the electronic spin acting on the spin of the nucleus. The splitting of the energy levels is represented by the hyperfine Hamiltonian

$$\hat{H}_{\text{hf}} = \hat{A}\mathbf{I} \cdot \mathbf{J}, \tag{2.16}$$

with $\hat{A}$ the hyperfine structure constant, $\mathbf{I}$ the operator for the nuclear spin and $\mathbf{I}$ the operator for the electronic angular momentum. Expressing $\mathbf{I}$ and $\mathbf{J}$ in terms of the operator for the total angular momentum, $\mathbf{F}$,

$$\mathbf{F} = \mathbf{I} + \mathbf{J}, \tag{2.17}$$

a scalar expression can be found for the product of $\mathbf{I}$ and $\mathbf{J}$, which reduces equation 2.16 to

$$\hat{H}_{\text{hf}} = \frac{\hat{A}}{2}\left[F(F+1) - I(I+1) - J(J+1)\right]. \tag{2.18}$$

As alkali atoms in their ground state have $J = S = 1/2$, the energy associated with the splitting between $F = I + 1/2$ and $F = I - 1/2$ is

$$\Delta E_{\text{hf}} = \left(I + \frac{1}{2}\right)\hat{A}. \tag{2.19}$$

In addition to the hyperfine interaction, splitting of the states also occurs due to the Zeeman effect. Whenever an external magnetic field is applied, the nuclei and electrons start interacting with it, giving rise to a Zeeman energy. The interaction Hamiltonian then becomes

$$\hat{H}_{\text{int}} = \hat{H}_{\text{hf}} + \hat{H}_{Z_{\text{el}}} + \hat{H}_{Z_{\text{nuc}}} \tag{2.20}$$

$$\hat{H}_{\text{int}} = \frac{\hat{A}}{2}\left[F(F+1) - I(I+1) - J(J+1)\right] + g\mu_B B J_i - \frac{\mu}{I} B I_i, \tag{2.21}$$

where g is the Landé factor, μ_B is the Bohr magneton, B is the magnetic field and subscript $i \in \{x, y, z\}$ denotes the direction in which the magnetic field is applied.

The splitting of the energy levels of atoms is used for trapping. In a magneto-optical trap (MOT), atoms are trapped in a quadrupole magnetic field and a series of laser beams, exerting a radiation pressure. The re-absorbing and emitting of photons cools down the atoms. While applied radiation pressure from the laser beams mostly contains the atoms, random walk might cause atoms to escape the trap. To prevent this, a magnetic gradient is applied to keep the atoms in the centre of the trap. Section 3.1 discusses MOTs in more detail and explains how they are used to cool ^{87}Rb.

2.2.2 Optical dipole trapping

Trapping using radiation pressure, as described in section 2.2.1 allows for traps with great trapping depths, with a typical depth of a few Kelvin. The near-resonance operating range, however, limits the trap performance. The strong optical excitation limits low trap temperatures, the density is limited by radiation trapping and light-assisted inelastic scattering, and lifetimes are on the order of microseconds. Optical dipole traps (ODTs) [19] rely on the electric dipole interaction with far-detuned light. These traps are generally much weaker and have typical trap depths in the order from nK to mK. The lower trap depth allows for lower temperature condensates and the nature of the dipole interaction allows the atoms to be trapped in arbitrary geometries.

Upon placing an atom in an electric field, $\mathbf{E}(\mathbf{r}, t) = \hat{\mathbf{e}} E_0(\mathbf{r}) \exp(-i\omega t) + h.c.$, the field induces an atomic dipole moment, $\mathbf{p}(\mathbf{r}, t) = \hat{\mathbf{e}} p_0(\mathbf{r}) \exp(-i\omega t) + h.c.$, oscillating at the driving frequency, ω. The amplitude of the dipole moment and electric field are related by [20]

$$p_0 = \alpha(\omega) E_0, \tag{2.22}$$

with α the complex polarisability.

The interaction potential is proportional to the time average of the induced dipole moment and the electric field [19],

$$U_{\text{dip}} = \frac{1}{2}\langle \mathbf{pE} \rangle = \frac{1}{2\varepsilon_0 c} \text{Re}\left(\alpha(\omega)\right) I, \tag{2.23}$$

with ε_0 the vacuum permittivity and c the speed of light. $I = 2\varepsilon_0 c \left|E_0\right|^2$ is the intensity of the electric field. The factor $1/2$ takes into account that the dipole moment is induced and not permanent.

The force exerted on the atom by the dipole field comes from the gradient of the interaction potential

$$\mathbf{F}_{\text{dip}}(\mathbf{r}) = -\nabla U_{\text{dip}}(\mathbf{r}) = \frac{1}{2\varepsilon_0 c}\text{Re}\left(\alpha(\omega)\right)\nabla I(\mathbf{r}). \tag{2.24}$$

The potential energy of the atom in the dipole field is thus proportional to the intensity $I(\mathbf{r})$ of the field and the force exerted on the atom is proportional to the gradient of the intensity $\nabla I(\mathbf{r})$.

For most of the alkali atoms, the polarisability can be found to good approximation by treating the valence electron as a driven oscillator. From the classic equation of motion and substituting Equation 2.22, the polarisability is found to be

$$\alpha = \frac{e^2}{m_e}\frac{1}{\omega_0^2 - \omega^2 - i\omega\Gamma_\omega}, \qquad \Gamma_\omega = \frac{e^2\omega^2}{2\pi\varepsilon_0 m_e c^3}, \tag{2.25}$$

with e the electron charge, m_e the electron mass, ω_0 the resonance frequency of the oscillator and Γ_ω the damping rate due to radiative energy losses. For the on-resonance damping rate $\Gamma = \left(\omega_0/\omega\right)^2\Gamma_\omega$, the polarisability then becomes

$$\alpha = 6\pi\varepsilon_0 c^3 \frac{\Gamma\omega_0^2}{\omega_0^2 - \omega^2 - i(\omega^3/\omega_0^2)\Gamma}. \tag{2.26}$$

By describing the electron in a two-level system, the decay rate Γ depends on the matrix elements of the ground and excited state. The classical approximation, however, agrees with the semi-classical two-level system within a few percent. Only when the excited state gets strongly populated, for example at high intensities of the driving field, Eq. 2.26 is no longer valid. Since most ODTs work with far-detuned light, saturation generally is very low, making Eq. 2.26 a good approximation.

Substituting the obtained result of Eq. 2.26 in Eq.2.23 and applying the rotating-wave approximation, the relevant potential energy of the atom due to the dipole field can be found:

$$U_{\text{dip}} = \frac{3\pi c^2}{2\omega_0^3}\frac{\Gamma}{\Delta}I(\mathbf{r}), \tag{2.27}$$

with $\Delta = \omega - \omega_0$ is the detuning from the atomic resonance frequency. For a laser with a frequency lower than resonance, a red-detuned laser ($\Delta < 0$), the potential is negative, and the atoms are attracted to the field. For frequencies higher than resonance, blue-detuned lasers ($\Delta > 0$), the potential becomes positive and the atoms are repulsed by the field.

Second-order time-independent perturbation theory can be used to apply Eq. 2.27 to the hyperfine states of the alkali atoms used in ultracold atom experiments. The potential of a ground state with total angular momentum F and magnetic quantum number m_F is then

$$U_{\mathrm{dip}}(\mathbf{r}) = \frac{\pi c^2 \Gamma}{2\omega_0^3} \left(\frac{2 + \mathcal{P} g_F m_F}{\Delta_{2,F}} + \frac{1 - \mathcal{P} g_F m_F}{\Delta_{1,F}} \right) I(\mathbf{r}), \tag{2.28}$$

with g_F the Landé factor, $\mathcal{P}$ the laser polarization (with $\mathcal{P} = 0, \pm 1$ for linearly and circularly polarised light) and $\Delta_{2,F}$, $\Delta_{1,F}$ the energy splitting between the particular ground state ${}^2S_{1/2}, F$ and the centre of the hyperfine split ${}^2P_{3/2}$ and ${}^2P_{1/2}$ excited states, respectively (see Fig. 3.2). The terms between brackets thus represent the contributions from the D_2 and D_1 lines to the dipole potential.

The dipole potential (Eq. 2.28) is useful for simulating ODTs. Various properties of optical traps can be obtained from this equation, such as the trap depth and the trap frequency. In Chapters 4 and 5, Eq. 2.28 is used for designing and characterization of the dipole trap developed in this thesis.

3
A Versatile BEC Apparatus

This chapter describes the process of experimentally creating a BEC using the experimental apparatus at UQ. In Section 3.1, the background from Sec. 2.2 is applied to describe the cooling and trapping of the ^{87}Rb atoms from initial cooling to condensation. Section 3.2 describes the trap potential which confines the atoms horizontally and how this potential is used for imprinting patterns and currents for dynamic control of BECs. In the last section, Sec. 3.3, techniques for imaging BECs are described. Two common imaging techniques, absorption and Faraday imaging are described. During the project, an improved method of Faraday imaging, called phase contrast Faraday imaging, was implemented and used. The last section describes the necessity of using this technique and how Faraday images are processed to obtain data that is proportional to the atomic density.

3.1 Creation of Bose-Einstein condensates

To observe a phase transition to Bose-Einstein condensation of atoms, particles have to reach sufficiently low temperatures. While cooling and trapping could in principle be done completely with the optical traps in which the experiments are performed, doing so would require incredibly high-power lasers, as dipole trapping happens far off-resonance. As such, it is more desirable to cool atoms to sufficiently low temperatures using other methods first, before transferring to optical dipole traps and evaporating the atomic cloud into Bose-Einstein condensation.

The first step in cooling the atoms is Doppler cooling in a MOT. The ^{87}Rb atoms are transferred to the 2D MOT of the vacuum system, depicted in Fig. 3.1. The 2D MOT consists of two pairs of counter-propagating beams that realise transverse cooling of the ^{87}Rb vapour. The atoms are mainly cooled from absorbing and remitting of photons, as explained

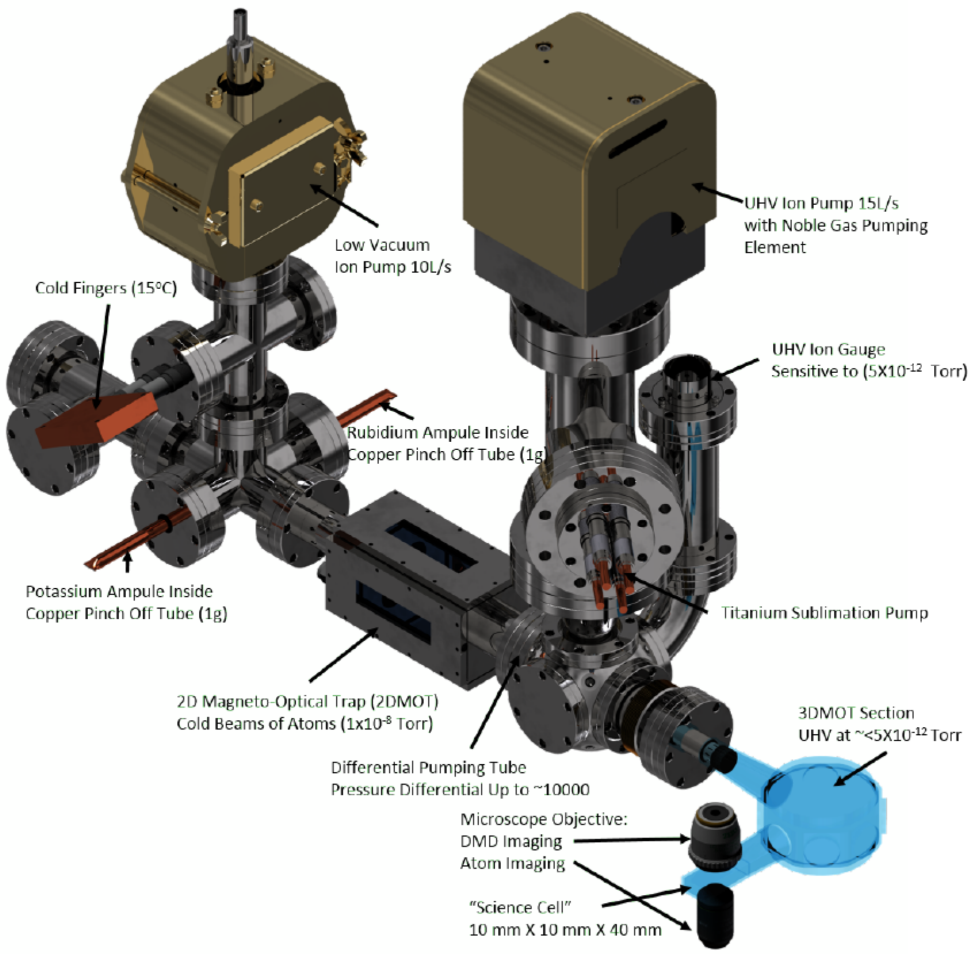

FIGURE 3.1: The vacuum system of the UQ BEC experiment utilized in this thesis. ^{87}Rb is transferred into the 2D MOT and cooled. The atoms are then transferred to a higher vacuum and are cooled down to temperatures slightly above the critical temperature in the 3D MOT. After transfer to the "Science Cell", the hottest atoms are evaporated and Bose-Einstein condensation is achieved. Retrieved from "Transport and Turbulence in Quasi-Uniform and Versatile Bose-Einstein Condensates", G. Gauthier, University of Queensland [21].

below. The magnetic field prevents atoms from escaping the optical beams through a random walk and additionally provides a small degree of cooling. This results in a beam of atoms that propagates through the differential pumping tube to the ultra-high vacuum side of the vacuum system. To facilitate this transfer, a near resonance 'push beam' is used. The force gradient from the radiation pressure pushes the atoms to the ultra-high vacuum. The 3D MOT is a glass octagon in which the atoms are irradiated from all six spatial directions. The atoms are cooled to the Doppler limit of approximately $T_{\mathrm{D}} = 146\,\mu$K. At this point, about 3^9 atoms are trapped. When this temperature is reached, the atoms are magnetically trapped and transferred to the "Science Cell" in which our experiments are performed. In the Science Cell, evaporative cooling is used to cool the atoms below critical temperature.

For cooling the atoms in the 2D and 3D MOT, the D_2 transition lines are used (see Fig. 3.2). The optical cooling laser drives the $5^2S_{1/2}|F=1\rangle \rightarrow 5^2P_{3/2}|F'=3\rangle$ transition with circular polarization $\sigma_\pm$. This forms a closed transition between $5^2S_{1/2}|F=1, m_F=\pm 2\rangle \rightarrow 5^2P_{3/2}|F'=3, m_{F'}=\pm 3\rangle$. The selection rules do not permit atoms which are initially in the $5^2S_{1/2}|F=1\rangle$ state to be pumped to the $5^2P_{3/2}|F'=3\rangle$ state. As such, a repump beam is used to facilitate the $5^2S_{1/2}|F=1\rangle \rightarrow 5^2P_{3/2}|F'=2\rangle$ transition. Through spontaneous emission, atoms in this state will decay into either the initial state used for the cooling transition, $5^2S_{1/2}|F=2\rangle$, or back into the $5^2S_{1/2}|F=1\rangle$ state, after which they will be repumped again. This creates a closed-loop cooling cycle.

After magnetic transfer to the Science Cell, the field is left on and microwave (MW) evaporation [22] is used to cool the atoms down to $\sim 15\,\mu$K. During evaporation, the magnetically trappable $5^2S_{1/2}|F=1, m_F=-1\rangle$ to the magnetically untrappable $5^2S_{1/2}|F=2, m_F=-1\rangle$ transition is used to drive the hottest atoms out of the trap. After 4 s, an atomic cloud of $1.5-2\cdot 10^8$ atoms remains. Condensation cannot be achieved through MW-evaporation due to Majorana losses [23] which occur in the zero of the quadrupole trap. At this point the quantization of the atoms becomes undefined, which can transition atoms to untrappable states.

To overcome this issue, the magnetic field gradient is ramped down and the atoms, which

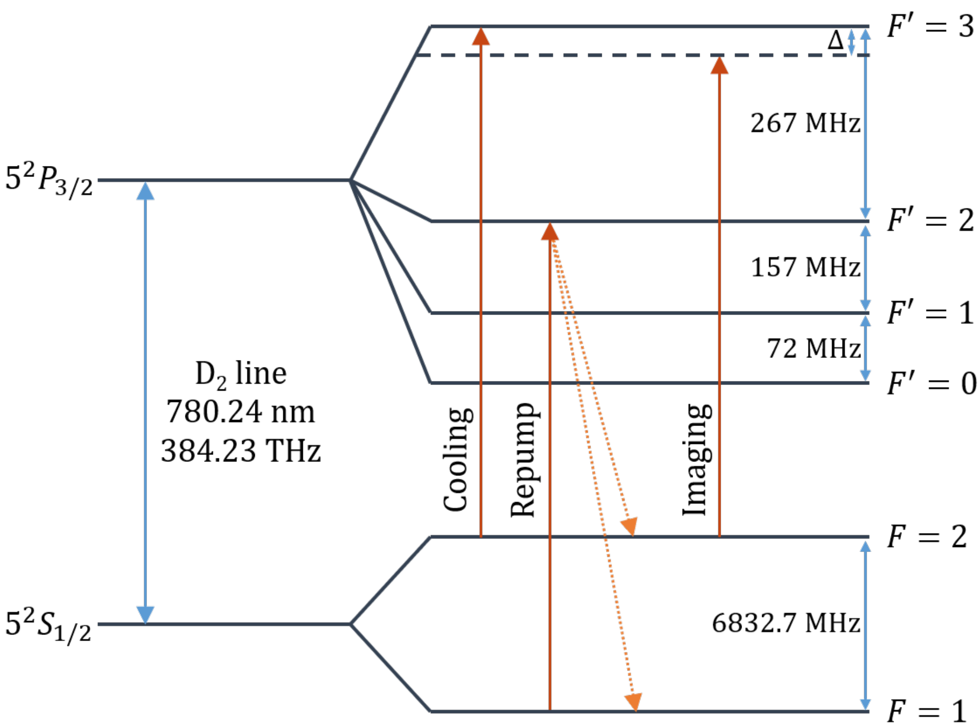

Figure 3.2: The hyperfine structure of ^{87}Rb. The D_2 line is the transition between the ground state $5^2S_{1/2}$ and the $5^2P_{3/2}$ excited state. The hyperfine substates are utilized for trapping and cooling of atoms.

fall down due to gravity, are transferred into an ODT without heating. Approximately $3 - 4.5 \cdot 10^6$ atoms are loaded into the ODT at a temperature of $4.5\,\mu$K. The decrease in temperature after transfer is due to higher dispersion of hot atoms. The temperature of the cloud is further decreased through optical evaporation, which is done by ramping down the power in the ODT. This causes the hottest atoms to be expelled from the trap. At $T = 450\,$nK, just above condensation temperature, the atoms are finally transferred from the ODT to a red-detuned 1064 nm beam focussed in the vertical direction and collimated in the horizontal direction. After transfer to this red-sheet beam, optical evaporation takes place in this trap until the condensation temperature of $\sim 300\,$nK is reached. Near the end of optical evaporation in the sheet beam trap, the DMD potential is ramped on, to provide horizontal confinement. After condensation, a cloud of $3 - 4 \cdot 10^6$ atoms with a condensate fraction of $> 85\%$ is obtained.

3.2 Configuring BECs with Digital Micromirror Devices

In order to perform transport and turbulence experiments, dynamic control of the condensate is required. Over recent years, spatial light modulators (SLMs) have been significantly advanced and have shown to be a very useful tool in optical manipulation and trapping of atoms [24]. A disadvantage of SLMs is that they operate in the Fourier plane and as a result, simple manipulations in the amplitude may require a lot of computational power. An increasingly more common method for dynamic control in cold atom experiments is through the use of a two-dimensional array of controllable mirrors, a digital micromirror device (DMD), as implemented at UQ [3].

The use of DMDs allows for easy amplitude control of light and offers fast refresh rates (20 kHz) at high spatial resolutions. The DMD used at UQ has a resolution of 1200×1920 mirrors. After loading atoms into the red sheet-trap, the DMD light is ramped on. A blue-detuned 532 nm laser is used to print a pattern into the condensate, which acts as a repulsive potential. Using this technique, any arbitrary potentials can be printed into the BEC. An example of early work with the DMD is shown in Fig. 3.3(a). As the mirrors can only be turned on or off, in principle it would only be possible to create a binary pattern. However, since light deflected from a single mirror undergoes diffraction, individual mirrors are not resolved by the imaging system, meaning multiple mirrors contribute to each spot.

Through turning off mirrors that illuminate the same spot on the atom plane, smooth potentials can be formed using the Floyd-Steinberg algorithm. In an ongoing investigation at UQ, this algorithm is used to create a smooth potential using a feed-forward algorithm [21], which predicts which mirrors to turn on and off based on data acquired in previous experimental sequences. This allows to create smooth potential wells or more complicated patterns, as depicted in Figure 3.3(b).

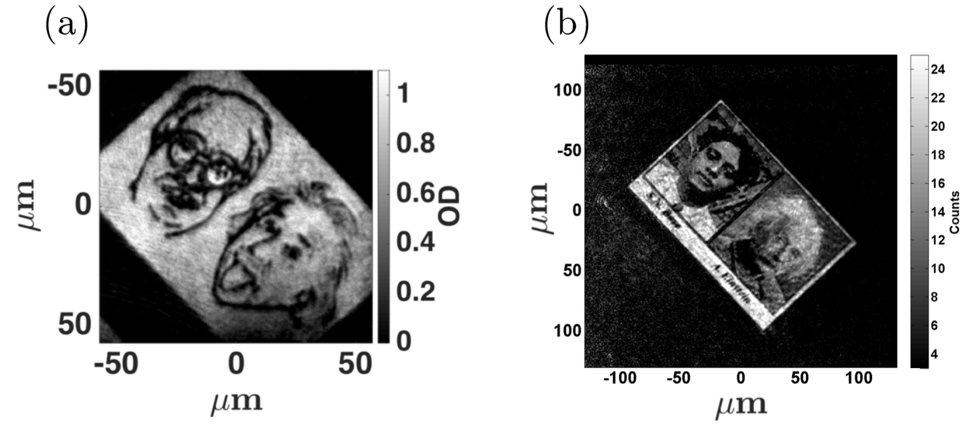

Figure 3.3: Imprinted Bose and Einstein in a Bose-Einstein condensate. (a) shows Bose and Einstein as a binary array and (b) shows the implementation of the Floyd-Steinberg with feed forward algorithm to create arbitrary, smooth potentials.

3.3 Imaging techniques for Bose-Einstein Condensates

In cold atom experiments, various techniques are used to image the BEC. The most common and simple one is through absorption imaging. Another well-known technique is Faraday imaging. The experiment at UQ utilizes both of these imaging techniques, absorption imaging is used when the BEC is imaged from the side and, depending on the number of atoms in the trap, either Faraday or absorption imaging is used when the atoms are imaged from the top.

To perform absorption imaging, a probe beam is used which drives the $5^2S_{1/2}|F=2\rangle \rightarrow 5^2P_{3/2}|F'=3\rangle$ transition and is detuned by Δ (see Fig. 3.2). The beam is detuned to prevent saturation on resonance. As the imaging light excites the atoms and is therefore scattered, a particular dark spot in the image is visible at which the atoms are located. The attenuation of the light by the atoms is given by the Beer-Lambert law. Using the Beer-Lambert law, the column density of an image can be obtained and from that the atomic density. To remove background noise and obtain an image of the cloud, three images are taken. One without any imaging light, a second one with imaging light but without atoms and a third one with imaging light and atoms.

A downside of using absorption imaging is that it relies on the scattering of photons. Due to optical pumping, acquired images are often blurred as a result of the radiation pressure that pushes the atoms out of the plane of focus. As such, it is often difficult to see small features in the condensate. Faraday imaging [25] overcomes this issue, as the measured signal relies on the phase-information of the probe beam, such that no optical pumping is required. The signal changes as the square of the column density, which makes this imaging technique much more sensitive to small features in the condensate.

When considering linearly polarised light as a superposition of circularly polarised light, each of the circulations experiences a different phase shift when passing through the atomic cloud. This leads to a rotation of the linearly polarised light by the Faraday angle, θ_F. The intensity fluctuation is obtained by transmitting the Faraday light through a polariser. The intensity is found to be $I_s(\mathbf{r}) = I_0 \cos^2\theta_\mathrm{F}(\mathbf{r})$.

The very nature of Faraday imaging also poses why it is not always the preferred method of imaging. As the signal changes with the square of the density, it is challenging to image clouds with low atom numbers. This poses an issue in experiments in which a large condensate area is required and small features have to be clearly distinguishable, as in the superfluid Reynolds number experiment, discussed in Chapter 6. The issue of using Faraday imaging in a condensate with a limited number of atoms was first overcome in a ^{7}Li BEC by the group of Hulet [26]. Because of the effectively attractive interactions between ^{7}Li atoms, many-body theory predicts the occupation number of ^{7}Li BECs are limited to only 1400 atoms. To use Faraday imaging at low densities, Hulet's group implemented a phase contrast technique can be used which enhances the signal. In this phase contrast technique, the waveplate for Faraday imaging is rotated slightly, such that the probe beam becomes elliptically polarised. One of these polarisations acquires a phase shift, while the other does not. Upon recombination at the polariser, both beams combine and interfere, producing the phase-contrast image. During the work for this thesis, this technique was implemented. The Faraday angle (and hence the polarization of the probe beam) is slightly modified, which adds a number of non-linear terms to the detected intensity distribution,

$$I_s(\mathbf{r}) = I_0 \left[\cos^2\theta + \frac{\sqrt{3}}{4}\phi(\mathbf{r})\sin 2\theta - \frac{3}{16}\phi(\mathbf{r})^2\cos 2\theta\right], \tag{3.1}$$

in which θ is the angle between the initial polarization of the probe beam and the polariser (or waveplate) axis and $\phi(\mathbf{r})$ the phase-contrast signal. In regular Faraday imaging, only the first term is taken into account as the phase-contrast signal is approximately zero. The signal $\phi(\mathbf{r} = \{x, y, z\})$ is related to the atomic density by

$$\phi(x, y, z) = -\left(\frac{\sigma_0}{2} + i\frac{\alpha}{2}\right)\int \mathrm{d}z\, n(x, y, z)\frac{\Gamma}{2\Delta + i\Gamma}, \tag{3.2}$$

in which σ_0 is the absorption cross-section, α is the optical density and Γ is the transition linewidth.

The number of atoms using Faraday imaging with phase-contrast is therefore found by solving Eq. 3.1 for $\phi(\mathbf{r})$ and solving 3.2 for $N = \int dz\, n(x, y, z)$. To investigate properties such as the flatness of the trap (see Sec. 6.1), the Faraday images have to be converted to data which scales linearly with the atomic number.

4

Experimental Design

One of the properties of atoms that is widely used for trapping them is their induced dipole moment upon interaction with light. An easy way of exploiting this property is by focussing a red-detuned laser on the location at which the atoms are to be confined. The high power at the beam's waist will act as an attractive potential in which the atoms are attracted to the centre. While a simple method, using a red-detuned source also brings various drawbacks. One of these drawbacks if that for sufficiently strong traps, atoms which are not part of the condensate, but which have sufficiently low energy are still attracted by the trap. These thermal atoms can float outside of the DMD-potential and introduce noise on measurements. Moreover, the use of a focussed Gaussian beam as a trap has the drawback that the vertical trap confinement has to be sacrificed for a large trap area, as the vertical waist of the beam depends on the Rayleigh length of the beam. This part of the thesis discusses the realization and characterization of a new, blue-detuned trap, which overcomes these issues. Because of its repulsive nature, thermal atoms are expelled from the trap. Furthermore, by shaping the trap using two interfering beams, atoms are confined in the fringes, and the vertical confinement can be controlled by adjusting the fringe spacing.

In Section 4.1, the working principles behind the blue-detuned optical lattice are discussed. Section 4.2 discusses the specific setup built at UQ in detail. A brief explanation of the setup can be found in the summary at the beginning of the section. The rest of the section goes through the setup and discusses all the major components. Section 4.3 discusses how the fringe vibrations are stabilized using a feedback system, which is unique to the UQ setup. The fringe fidelity of the trap plays a large role in the lifetime of the BEC in the trap. Section 4.4 discusses how the fringe fidelity is held constant in our setup by ensuring the polarisation of the light in the setup does not drift when using polarisation maintaining fibres (PMFs).

4.1 Trapping atoms in a blue-detuned optical lattice

Sheet-shaped focussed beams are easy to realise traps. Through use of cylindrical lenses, the horizontal waist of the beam can be expanded and upon focussing through a lens, a sheet-shaped trap is formed. When a red-detuned source is used, atoms will be trapped in the sheet due to its attractive potential, as described in Section 2.2.2. Red-detuned traps are often favoured over blue-detuned traps, due to their repulsive nature, traps are more complex as they require multiple beams to prevent atoms from escaping in horizontal and vertical directions. The downside of using a red-detuned focussed beam as trap it the vertical trap frequency and depth highly depend on the vertical beam waist and Rayleigh length. To obtain a high trap frequency, a small vertical waist is required and as a result, the beam will have a small Rayleigh length, making the beam very anisotropic in both horizontal directions. A quasi 2D trap is achievable using a focussed sheet-beam but achieving a true 2D trap for a large condensate requires another method of trapping.

In 2017, Ville et al.[8] proposed a blue-detuned ODT using an optical lattice to confine the atoms vertically. Another beam used to confine the atoms horizontally and to imprint currents using a DMD. When considering the Science Cell in Figure 3.1, the optical lattice confines the atoms vertically by illumination from the side. The horizontal confinement is achieved by illumination from the top, through the DMD imaging objective. The lattice is created through the interference of two identical blue-detuned beams. The atoms are confined in the nodes of the lattice. The trap depth, i.e. the depth of the potential at a position, $\mathbf{r}$, depends on the intensity of the light, as obtained from Equation 2.28. If we assume the trap is harmonic, the trap frequency is proportional to the second spatial derivative of the potential, as will be discussed in more detail in Chapter 5. The trap frequency can therefore be controlled by changing the intensity of the light or by adjusting the lattice spacing. The lattice spacing is changed by adjusting the beam separation

$$\lambda_{\text{lattice}} = \frac{\lambda_{\text{light}}}{(2n\sin\theta)}, \qquad \theta = \arctan\left(\frac{d}{2\,f_{\text{final}}}\right), \tag{4.1}$$

with λ_{light} the laser wavelength, n the refractive index, d the centre to centre beam separation and f_{final} the focal distance of the final lens in the setup (see Fig. 4.3).

Theoretically, the lattice node can be made as small as $\lambda_{\text{light}}/2$ at $\sin\theta = 1$. To achieve this one is often limited by technical limitations: θ depends on the beam separation, d, the lattice spacing is limited by the aperture of the final lens, f_{final} and the size of the beamsplitters that set the beam separation, as will be discussed in Sec. 4.2. The ability to create these lattice nodes inside of the Gaussian envelope allows one to choose a vertical beam waist, and as such, a Rayleigh length that is sufficiently large to trap large condensates, while still having control over how tightly confined the atoms are in the vertical direction.

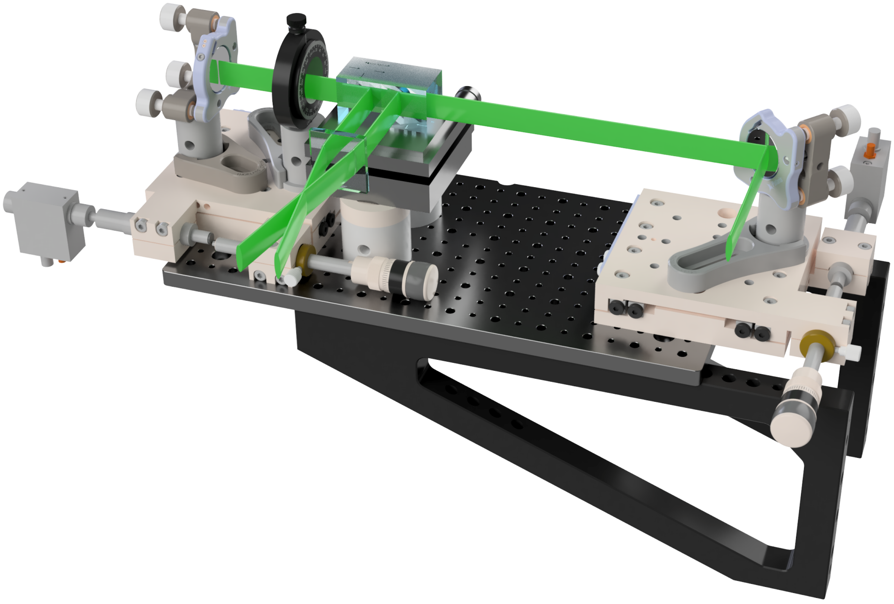

Figure 4.1: The experimental setup for creating two identical beams. A single incoming 50/50 polarised beam is split using two polarizing beamsplitters. Using a lens both beams can be recombined to create an optical lattice.

4.2 Experimental Setup Summary

This section summarizes the experimental setup created for the optical lattice and features all the major components. A step-by-step description of the function of each component can be found in Appendix A.2.3. The optical lattice setup built at UQ consists of various components, which can be split up into four parts: The optics on the bottom optical table (see Fig. 4.2), the tower, the optical path which transmits the light to the atoms, and the feedback path (see Fig. 4.3).

4.2.1 Bottom optical table

On the bottom table, the laser head is mounted. The 532 nm laser light is blue-detuned for the ^{87}Rb atoms and is used for both the optical lattice and the DMD potential. Using a waveplate and polarizing beamsplitter (PBS), the light at (1) is split into a 3W beam for the DMD potential and a 7W beam for the optical lattice. The light is transmitted through an AOM at (2). This AOM diffracts the light into various diffraction orders and is used to control the intensity of the light in the path: Whenever high powers are required, most of the light will be transmitted through the first diffraction order and whenever low powers are required, most of the light is transmitted through the zeroth order, which is deflected onto a beam dump. The power in the path is measured at (11), see Fig. 4.3.

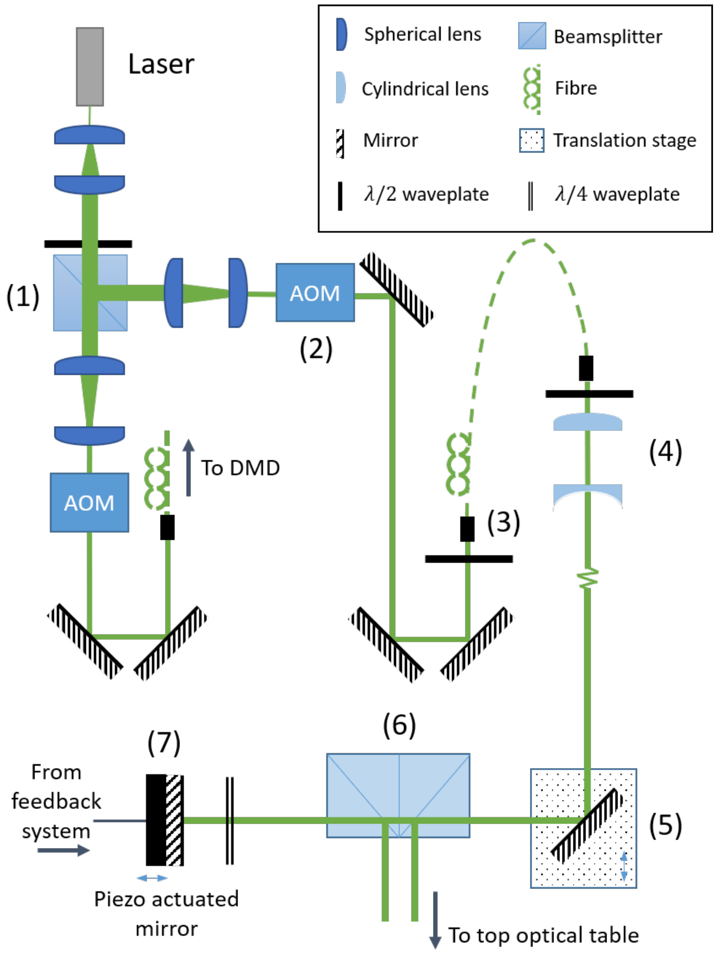

FIGURE 4.2: A diagram of all optical components found on the lower optical table. The light of the $\lambda = 532\,\mathrm{nm}$ is split into two different paths, the DMD setup path and the optical lattice.

The light is then transmitted through a fibre at (3). An optical fibre is used for two reasons: The fibre couplers act as a spatial filter and as such, any irregularities in the Gaussian beam profile we observed are induced by the AOM crystal are removed. Secondly, the fibre decouples the first part of the setup from the other components. Any misalignments or adjustments in optics before the fibre therefore do not result in misalignment of the optical lattice.

4.2.2 The tower

To prevent thermal lensing in the optical components, the beam is (vertically) expanded at (4), before being transmitted to the tower, shown in Fig. 4.3. The mirror at (5) is mounted on a translation state, which allows us to move the beam closer and further apart from the edge of the PBSs (6) and as such, to set the beam separation and the lattice spacing (see Eq. 4.1). To obtain a small beam separation, the beams have to be very close to the edge of the beamsplitters. To achieve this without the beams clipping over the sides of the PBSs, a small horizontal beam waist is required. As such, only the vertical waist is expanded at (4).

The light incident on the PBSs on the tower is 50/50 linearly polarised. As a result, 50% of the light is reflected from the first beamsplitter. The remainder of the light is transmitted through the second beamsplitter onto a mirror mounted on a piezoelectric actuator (7). This mirror is connected to our feedback system which ensures any vibrations in the optical lattice are corrected by locking the phase between both beams (for details, see Sec. 4.3). A $\lambda/4$ waveplate in front of the mirror rotates the beam's polarisation to be vertically polarised and as such, to be reflected from the top beamsplitter.

4.2.3 Top optical table

Both beams travel through the remainder of the system with a vertical polarisation. At (8) the light is split again using a PBS, but as the beams are vertically polarised, only a fraction is reflected onto the feedback path. The transmitted light travels to the atoms, but first has its waist reduced at (9). The final lens, f_{final}, at (10), vertically focusses the light on the

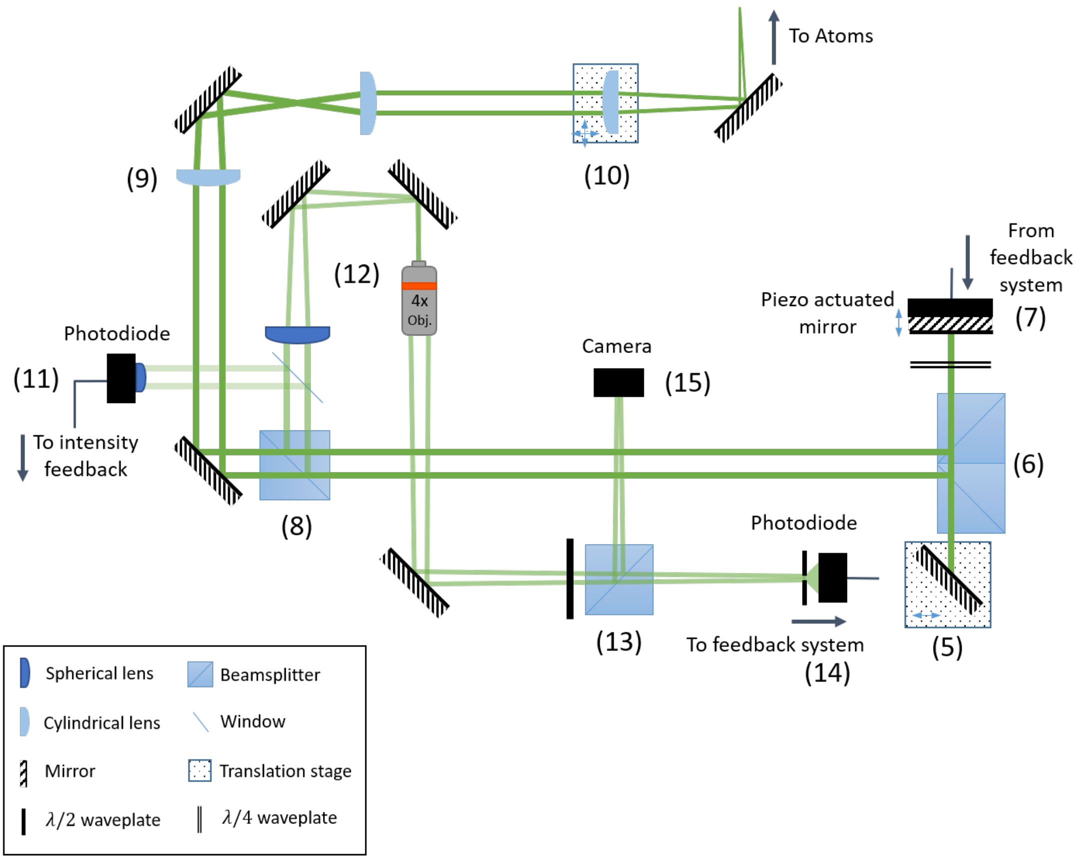

Figure 4.3: A diagram of all optical components found on the top optical table. After being split into two, the majority of the light is transmitted to the Science Cell. A fraction of the light is reflected to the path which ensures the phase-locking feedback in the system.

atoms, at which the beams will interfere and form the optical lattice.

The light which is reflected at (8) is partially used to control the intensity of the light in the lattice. A photodiode at (11) sends reads the power in the system and sends the measured signal to the AOM at (2). The remainder of the light in this path is used to send the input signal to the feedback system, using a pinhole and photodiode at (14), and to monitor the stability of the optical lattice using a camera at (15). In Section 4.3, our feedback system is described in detail.

The input power in the optical lattice path is $P_{\text{input}} = 7\,\text{W}$. Due to losses in the system, the total power, measured in (9) is $P_{\text{total}} \approx 2\,\text{W}$. For the given beam waist of $w_{(3)} = 1.38\,\text{mm}$ at the fibre coupler after (3), the final beam calculated beam waists at the atoms are $w_z = 25.6\,\mu\text{m}$ and $w_x = 1.23\,\text{mm}$ for the vertical and horizontal waist, respectively. We will see in Chapter 5 that these calculated values do not exactly match the measured waists at the atoms, and how that affects the trap frequency.

4.3 Phase locking using active feedback

A unique feature about the setup at UQ is the phase locking feedback system. This feedback system ensures any vibrations in non-common mode paths are corrected. Any vibrations in non-common mode paths result in a phase difference between both beams. As illustrated in Figure 4.4, a phase difference in the beams results in displaced fringes, and as such, random

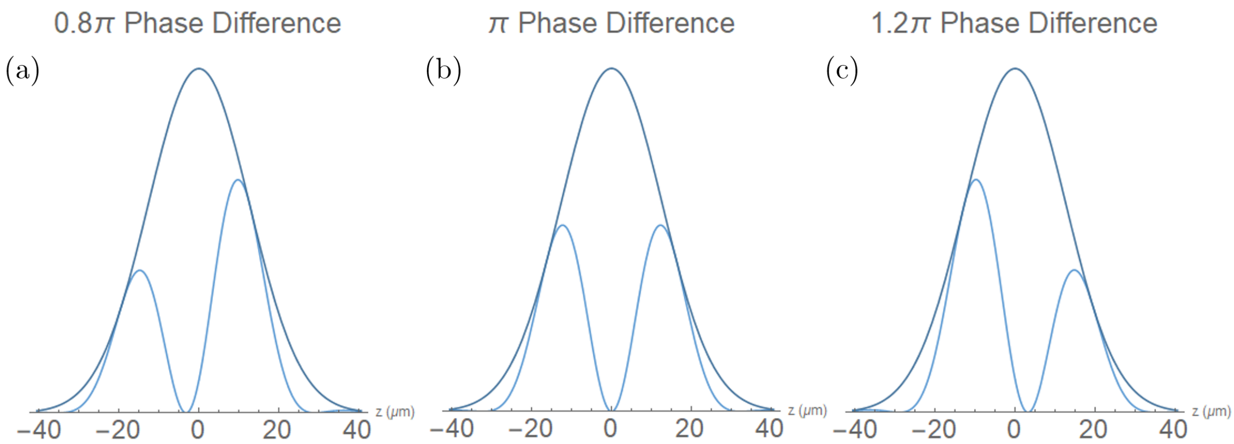

FIGURE 4.4: The optical lattice in the Gaussian beam envelope with various phase differences between top and bottom beam. (a) shows a phase difference of 0.8π between the beams, (b) is the default setting, to which the system is locked, which is a π phase difference and (c) shows a 1.2π phase difference. These phase differences correspond to a 52 nm vibration in the system for $\lambda_{\text{light}} = 532\,\text{nm}$. The most obvious feature is a the intensity mismatches between both fringes, which exerts a force on the atoms. Additionally, while the Gaussian envelope remains in the same position, the trap centre moves around. Vibrations at the trap frequency of the trap heat the atoms which reduces the BEC lifetime.

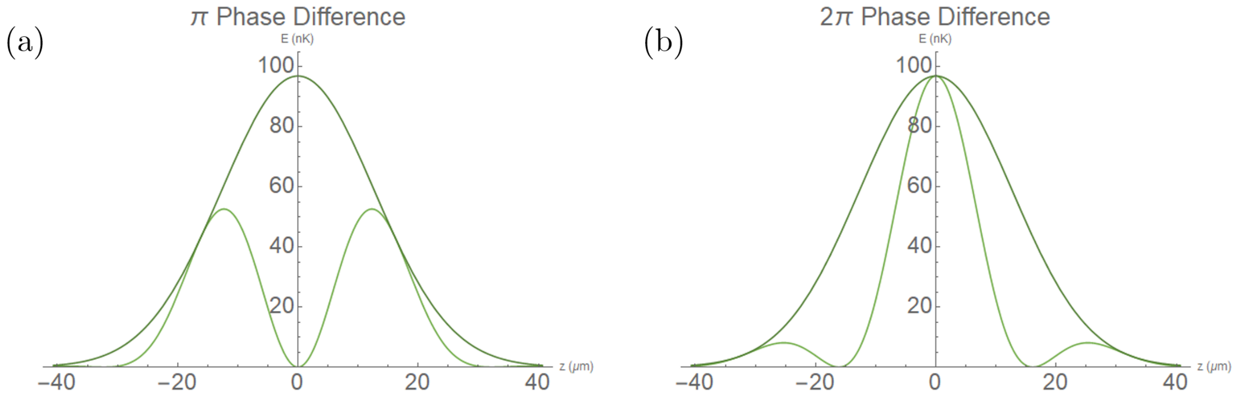

Figure 4.5: The trap depth of the optical lattice with (a) a π phase difference between both beams and (b) a 2π phase difference. While it is still possible to trap atoms in one of the minima in (b), the trap depth is much lower which results in a much lower trap frequency. The dark green line represents the Gaussian envelope in which the lattice is formed.

noise results in shaking of the lattice. If the frequency spectrum of the noise has any overlap with the trap frequency, the atoms heat up and escape the trap, resulting in a low trap lifetime. In Chapter 5, the lifetime of the trap with and without utilisation of the feedback system is compared.

While the main feature of the system is to actively lock-in the phase between both beams, it also allows one to configure the relative phase between both. To maximize the trap depth, the interference minimum is centred on zero. Although it is still possible to trap atoms at other interference minima, the trap depth is highest at the centre of the Gaussian envelope. Figure 4.5 illustrates the full in and out of phase picture of the trap.

The active feedback system consists of three components: The pinhole and photodiode, the PI-controller (proportional-integrator controller) and the piezo actuated mirror (see Fig. 4.3). The photodiode provides the signal for the error measurement, the PI-controller reads the signal and compares it to the locked-on signal value and sends a corrected signal[1] to the piezo actuator. The system is able to respond to fluctuations just over 12 kHz.

The signal acquisition for the feedback system works as follows: Two lenses are combined to focus the light and form an interference pattern on the pinhole. To get a high resolution, i.e. to measure only a small portion of the interference pattern, an interference pattern much larger than the pinhole is required. The two lenses are combined to have a focal distance of approximately 550 mm. Using Equation 4.1 we find a fringe spacing of $\lambda_{\text{lattice}} \approx 90\,\mu$m. The amount of power transmitted through the pinhole is detected by the photodiode and translated to a voltage. The relative phase difference between both beams is set by moving the offset of the piezoelectric actuator that drives the mirror. Figure 4.6 illustrates how this is achieved: When the phase difference is 2π, depicted in (a), the photodiode detects a maximum signal. The mirror is moved is shifted until a π phase difference is observed on the

[1] More commonly referred to as the 'error signal' by system and control engineers.

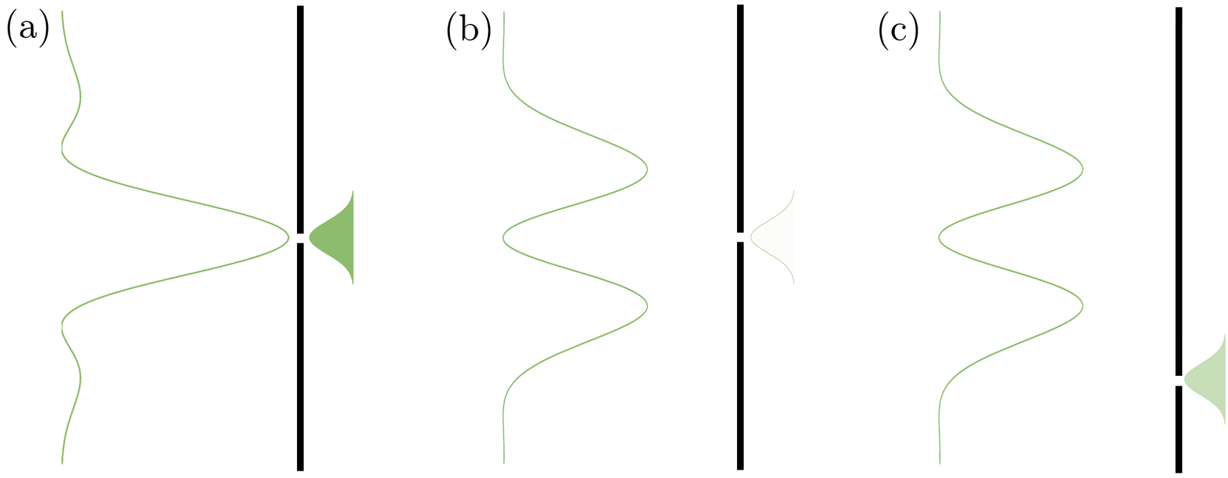

FIGURE 4.6: An illustration of how the relative phase difference between both beams is set and how the system is locked. Figure (a) shows the interference pattern with a 2π phase difference. The piezoelectric actuator which moves the mirror is then moved to obtain a phase difference of π (b). Once a dark fringe is in the centre of the Gaussian beam envelope, we move the pinhole to the side of the fringe, at which the derivative is largest and the lock is most effective (c).

camera. Once a dark fringe is located in the middle of the Gaussian envelope, the pinhole is moved to the side of the fringe, at which the system is locked.

The photodiode is connected to a Newport LB1005-S High-Speed Servo PI-Controller. The PI-controller features two input channels, a positive and a negative bias input channel. The negative input channel can be used to remove an offset signal or to remove any signal which is not to be corrected. This is useful when for example applying noise-correction on an AC-signal. Other than for inducing a perturbation in the system to measure the trap frequency (see Chapter 5), this channel is not used in day-to-day operation.

A useful feature of the PI-controller is the ability to sweep over a signal. When fed a periodic signal, as is done from our oscilloscope, a sweep can be turned on which drives the piezo actuator. Using this sweep, the input signal offset can be adjusted such that the controller locks-on to a value in the signal which has a large derivative. At this point, fluctuations from the original signal are more easily detected, ensuring better operation and error correction. The controller has two modes of operation, the low frequency gain limit (LFGL), which acts as an intermediate step before fully locking, and the lock-on mode. Once the lock-on point has been found, the LFGL mode can be switched on. At this stage the PI-filter can be set to the desired frequency and the gain can be increased to slightly below the point at which the piezo starts self-oscillating. The camera in the feedback path is used for setting and monitoring the lock.

In summary, the system is locked-on as follows: The relative phase between both beams is set to be π by moving the pinhole and output offset of the PI-controller. Once the camera shows the dark fringe is in the centre of the Gaussian envelope, we lock the PI-controller

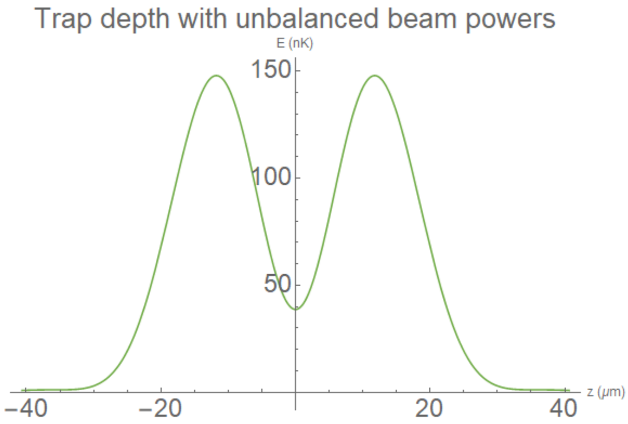

Figure 4.7: When the polarisation in one of the beams isn't equal to the other one, the power in the beams is not distributed equally. This results in a non-zero intensity point in the lattice. This means that in any point in the trap, a force is exerted on the atoms, resulting in a low lifetime.

to the point at which the derivative is the signal is the largest. This is the point at which fluctuations are the easiest to detect. After locking, gain is set slightly below the point of self-oscillating, which can be observed on the camera. The system is now ready for operation.

4.4 Polarisation-maintaining fibres

The main working principle of creating the optical lattice is creating an identical second beam through utilization of the polarisation of the initial beam. Because of the repulsive nature of the trap, lattice nodes with zero intensity are a requirement to achieve long BEC lifetimes in the trap. It is therefore crucial that the power in both beams remains equal. A mismatch in beam intensity results in a low fringe fidelity. Figure 4.7 shows a simulation of the trap potential in which one of the beams carries five times more power than the other, which results in a trap with a non-zero minimum. The power that is reflected into each beam at the PBSs (number (6) in Fig. 4.3) depends on the polarisation of the incident beam and has to be split 50/50 horizontally/vertically to equally distribute the power throughout the system. No polarisation drift over time is a requirement to the functionality of the optical lattice. As such, special considerations must be made to ensure the conservation of the polarisation in the system.

The fibres which uncouple the AOMs from the rest of the system, shown in Figure 4.2 are polarisation-maintaining fibres (PMFs). These fibres have a built-in birefringence to maintain the polarisation of incoming light, contrary to ordinary fibres, in which birefringence is undesired and induced by stress. The birefringence in regular fibres cause cross-coupling of power between both polarisations, which results in a not well-maintained polarisation. Provided the input polarisation is aligned with the birefringent axis, the polarisation is conserved [27].

Misalignment with the birefringence axis exerts itself in the setup by a slow drift in the polarisation when the fibre is heated up, i.e. when a large amount of optical power is coupled into the fibre. In the system, the drift can be seen as a shift in power distribution in the beams. As the fibre heats up, the polarisation changes until the fibre is completely heated up. Upon alignment with the birefringence axis, little to no change in polarisation is expected.

The degree of incoming which light which is aligned to the birefringence axis is quantitatively described by the polarisation-extinction ratio. The extinction ratio is measured by mounting a polariser or a waveplate in front of and after the optical fibre. By rotating the waveplate after the fibre and measuring the maximum and minimum power using a polariser mounted on a detector, the extinction ratio is obtained. In the setup at UQ, instead of placing a polariser in front of the detector, one of the beams on the upper table can be blocked to achieve the same effect, as the each of the PBSs only transmits one of the polarisations. The angle of the waveplate in front of the fibre is set and the waveplate after the fibre is rotated. The extinction ratio is calculated from the minimum and maximum power measured from rotating the second waveplate. The extinction ratio is then found by

$$\mathrm{ER} = 10 \log_{10} \left(\frac{P_{\mathrm{max}}}{P_{\mathrm{min}}} \right), \tag{4.2}$$

with P_{min} and P_{max} the measured minimum and maximum powers.

The procedure for matching the polarisation to the birefringence axis is as follows: At low power, the angle of the first waveplate is set. As a $\lambda/2$ waveplate is used, ideally only a quarter of the full rotation has to be scanned to find the lowest and highest extinction ratio. This waveplate is rotated in steps of 3°. The second waveplate is subsequently rotated to measure the power in the top beam. To achieve an extinction ratio greater than 20 dB, the misalignment must be less than 6° and to achieve an extinction ratio greater than 30 dB, the angular misalignment must be less than 1.8°. The power is measured using a high-power

θ (°)	P_{max} (mW)	P_{min} (mW)	ER (dB)
162 ± 0.5	61 ± 0.5	0.8 ± 0.1	-19 ± 0.5
165 ± 0.5	63 ± 0.5	0.6 ± 0.1	-20 ± 0.7
168 ± 0.5	65 ± 0.5	0.7 ± 0.1	-20 ± 0.6
171 ± 0.5	67 ± 0.5	0.5 ± 0.1	-21 ± 0.9
173 ± 0.5	66 ± 0.5	0.3 ± 0.1	-23 ± 1.4
174 ± 0.5	66 ± 0.5	0.4 ± 0.1	-22 ± 1.1
177 ± 0.5	68 ± 0.5	0.6 ± 0.1	-20 ± 0.7
180 ± 0.5	67 ± 0.5	1.1 ± 0.1	-18 ± 0.4
183 ± 0.5	66 ± 0.5	2.3 ± 0.1	-14 ± 0.2

TABLE 4.1: The extinction ratios found for different angular rotations of the $\lambda/2$ waveplate in front of the PMF. The polarisation of the incident beam is best for the highest extinction ratio. P_{max} and P_{min} are the maximum and minimum measured top beam power upon rotating the $\lambda/2$ waveplate after the optical fibre.

thermal sensor, while the bottom beam is blocked by a beam block at (4) in Fig. 4.3. The results of the measurement are shown in Table 4.1.

Upon finding the highest extinction ratio, the polarisation drift over time at high power is measured. This is expected to be minimal at the highest extinction ratio. To measure the drift over time, the top beam power has to be measured simultaneously as the power in both beams. The power in the top beam is measured after (4) and compared to the power in both beams, measured from the photodiode which controls the AOM power. The extinction ratio over time is not directly measured from this, as the power to voltage conversion in both detectors is different and the overall power in the feedback path is much lower. Instead, the drift is measured simply by dividing the top beam power over the total measured power. To record overall thermal drifts in the system, without correcting the power with the photodiode and AOM, the experiment is done two times: Once without locking the AOM to a certain high power and once with locking the AOM. Figure 4.8 shows the results of the measurement.

The least thermal drift is found for $\theta = 175 \pm 0.5°$, which is very close to the angular rotation at which the highest extinction ratio is found. The second waveplate is set to polarise the light 50/50% horizontally/vertically, to equally distribute the power when the beam is split. The fringe fidelity now remains unchanged to any perturbations to the fibre.

4.5 Conclusion

In this Chapter, the working principles behind the optical lattice were discussed. In Section 4.1, the advantages of using an optical lattice over a focussed beam sheet-trap were discussed and in Section 4.2 we demonstrated how an optical lattice is created experimentally. To ensure a long BEC lifetime in the trap, the lattice needs to be free from fluctuations. The realisation of an active feedback system to reduce vibrations in the lattice was demonstrated in Section 4.3. In addition to a vibration free system, it is also important to have a high fringe fidelity to achieve long condensate lifetimes. To ensure the power distribution in both beams remains equal over time, we implemented polarisation maintaining fibres in our system, described in Section 4.4.

With all these features implemented into the system, we can start characterizing the optical lattice trap. The next few Chapters will focus on the characterization of the trap. In Chapter 5, the lifetime of a BEC in the optical lattice is measured. We compare the condensate lifetime of the setup with the feedback system turned on and off, to demonstrate the necessity of using active lattice stabilization. Another important characteristic of the trap is the trap depth and frequency. As we have already seen in Section 2.1.3, many of the dynamic properties of the BEC depend on the frequency of the trap. In Chapter 5 we propose an experiment through which we can find the trap frequency of the system.

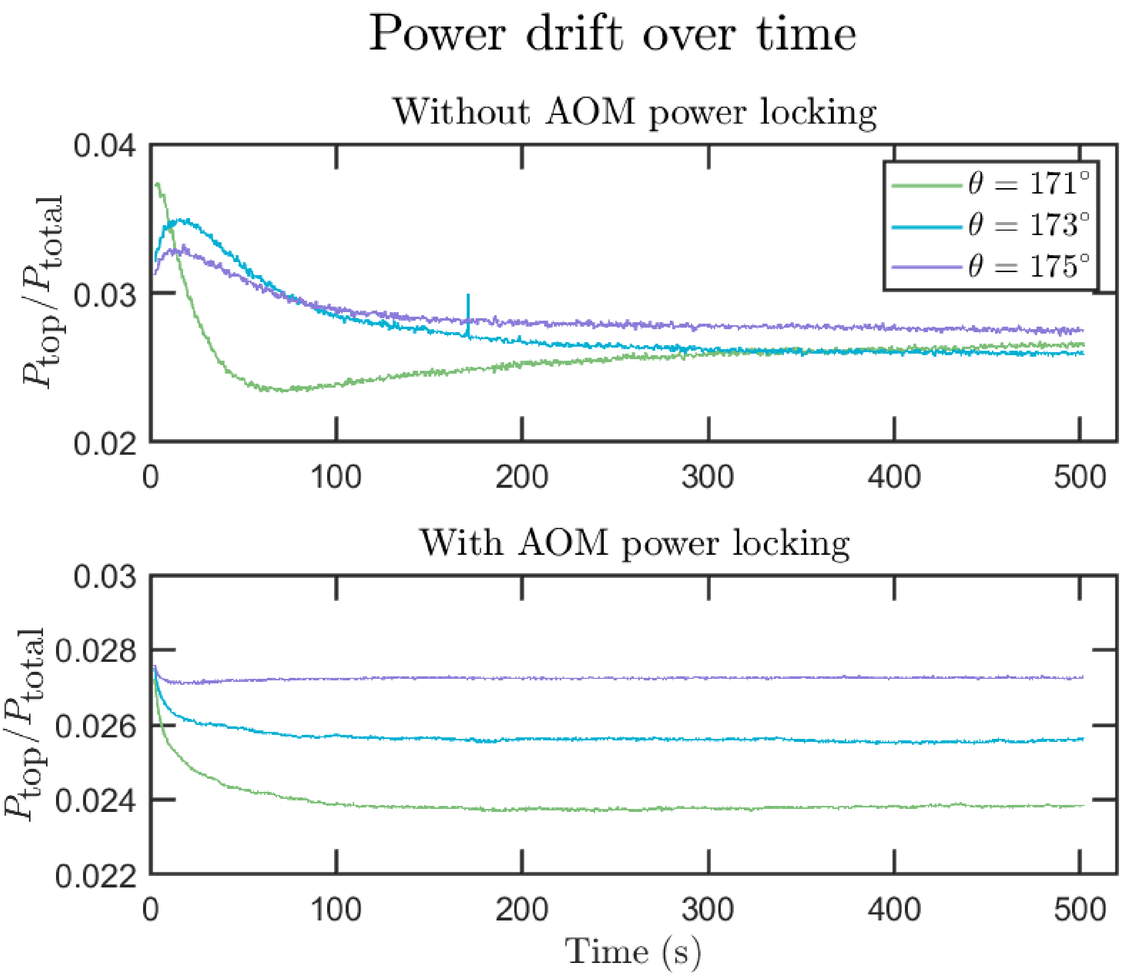

FIGURE 4.8: Power drifts due to fluctuations in the polarisation over time at high power. The different colours represent different angular rotations of the waveplate in front of the fibre, which correspond to different misalignments with the birefringence axis in the fibre. The top figure shows the drifts in power when the overall power of the light is not locked using an AOM, which shows thermal drifts in the system. In the bottom figure, the power is locked with an AOM. The least drift is found for $\theta = 175°$, at which the highest extinction ratio was found.

5

Characterization of the optical lattice

One of the key properties of experimental BECs are their lifetimes. The lifetime of a BEC depends highly on the type of condensate, with photon and exciton-polariton BECs having a lifetime of the order of picoseconds to nanoseconds [28, 29] and atomic BECs having lifetimes from seconds to minutes [3]. An atomic condensate with a lifetime of a few seconds or of a minute firstly depends on the quality of the vacuum system, but also on the trap in which the condensate is confined. In the first Section of this Chapter, the lifetime of the optical lattice trap is investigated. Section 5.1.1 describes the various loss mechanisms which affect the lifetime of an atomic condensate. In Section 5.1.2, the experimental sequence for measuring the lifetime is proposed and Section 5.1.3 discusses the results of the experiment.

The trap depth and frequency are important properties that affect the chemical potential, and as such, the dynamics of the BEC in trap. As seen in Chapter 2, the healing length, the speed of sound and the effective dimensionality depend on the chemical potential. As such, to accurately predict the behaviour of a trapped BEC, it is essential to have a good estimate of the trap frequency. In the second Section of this Chapter, an experiment that measures the trap frequency of the optical lattice trap is described. The most common method of doing so is using parametric heating, as discussed in Sec. 5.2.1. This method works well for attractive, harmonic traps. In this Chapter we demonstrate this method also works for repulsive, anti-harmonic traps, which are nearly flat. In Section 5.2.2, the trap depth and frequency of the trap are predicted using numerical simulations with the design parameters from Chapter 4. Section 5.2.3 discusses the experimental sequence of the proposed experiment and in Section 5.2.4, the results are presented and compared to the numerical simulations. The differences between the simulation and experimental data are discussed and future improvements to the trap to more accurately match the simulation with the experiment are proposed.

5.1 The lifetime of anti-harmonically trapped BECs

5.1.1 Background

Any BEC has a certain finite lifetime when trapped. The lifetime is a result of interparticle collisions with background atoms or molecules and is measured as the time taken to reach the 1/e level of initial atoms in the trap. Various collision processes must be considered for an accurate description of the atom number in the trap [30].

Interactions between trapped atoms and background atoms or molecules in the vacuum affect the lifetime considerably. Collisions between the higher energy particles in the vacuum and the trapped atoms allows for an inelastic momentum transfer. If the momentum transfer is too large, the trap depth may be too low to confine the atom any longer. Other heating processes, such as photon scattering or shaking of the atoms also limit the lifetime. All these processes are first order collision processes; the rate of atoms lost over time due to these interactions is linearly proportional to the number of atoms in the trap at time t.

Collisions between two atoms in the condensate, two-body collisions, can cause a redistribution of energy and convert internal energy into kinetic energy. The increase in kinetic energy may result in a loss of atoms if the trap depth is too low. Two-body interactions play a large role in multi-component and spin-polarized condensates [31], in which the scattering between different hyperfine states are present.

At high densities, such as after loading atoms into traps with high trapping frequencies, wherein all atoms are confined in one mode, three-body interactions must be considered. Three colliding atoms may form a diatomic molecule. The binding energy of the two atoms forming the molecule is transferred to the third atom, and both the molecule and atom are lost.

A description of the atom number in trap with these loss mechanisms is given by

$$\frac{dN}{dt} = -\Gamma N - \beta N^2 - \gamma N^3, \tag{5.1}$$

in which N is the atom number in the trap, Γ encompasses the BEC and background collision rate, as well as photon scattering, β is the two-body and γ the three-body collision rate.

All the experiments performed in this thesis are done in densities far below the threshold in which three-body interactions are relevant and to good extend, two-body interactions can be neglected. The lifetime in the optical lattice is dominated by photon scattering and collisions between BEC and thermal atoms. This gives the simple solution

$$N(t) = N_0 \exp\left(-\frac{t}{\tau}\right), \tag{5.2}$$

with $\tau = 1/\Gamma$ is the lifetime in the trap.

5.1.2 Experimental sequence

The atoms are initially transferred from the optical dipole trap to the red-detuned sheet trap with the DMD potential ramped on, as discussed in Chapter 3. The imprinted potential used for this experiment is a 50 μm radius circle. To achieve transfer with as little losses as possible, the red sheet trap power is ramped down equally as much as the optical lattice trap is ramped on. Once the atoms are transferred into the lattice, the lifetime measurement starts.

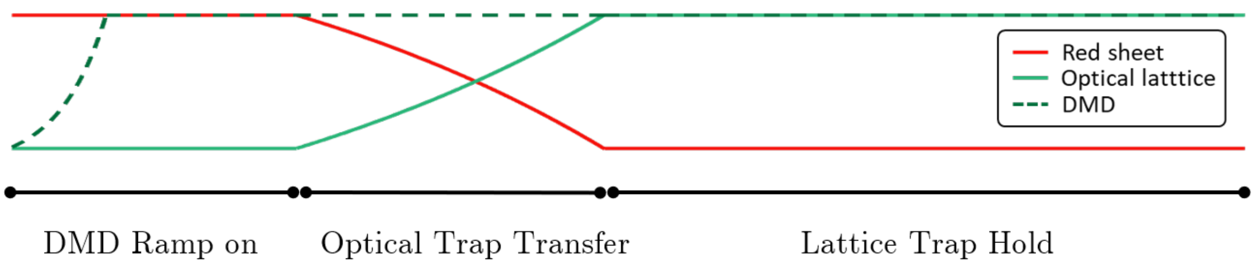

Figure 5.1: The experimental sequence for measuring the lifetime of the optical lattice. The measured time starts at the "Lattice Trap Hold" timestep.

The lifetime is determined by measuring the number of atoms in the BEC. This is done by imaging the cloud from the side. Imaging is done using absorption imaging, as discussed in Chapter 3; a beam probes the $5^2S_{1/2}|F = 2\rangle \rightarrow 5^2P_{3/2}|F' = 3\rangle$ transition. The lack of imaging light in a certain spot on the camera corresponds to the presence of the atomic cloud. The number of atoms in the cloud is then extracted using the integrated optical density and the absorption cross-section of the probed transition.

5.1.3 Results and discussion

Measurements are performed with the active phase-locking feedback (described in Sec. 4.3) turned on and off, to investigate the improvement in the lifetime with lattice stabilization.

The purple and green dots correspond to the mean of the experimental atom number data with and without feedback, respectively. The solid lines are fits to the data, using Eq. 5.2. The lines are fit using the full data set, instead of from the mean, to give each data point the same weight. This explains the slight overshoot in the fit without feedback.

A general higher uncertainty is found for the data in which no feedback is used. This is expected because of the irregular shaking of the lattice. The BEC lifetime in the trap without feedback is found to be $\tau = 2.9(8)\,$s and $\tau = 19(5)\,$s with active feedback, both at 95% confidence. The lifetime with feedback is slightly dependent on the tuning of the PI-controller lock. There was a clear distinction in the robustness of the lock just after the experiment had been turned on and after it had been running for a while. A possible explanation for that is the increase of the temperature in the box causing a drift in the alignment of the beam on the pinhole, and as such, the point to which the PI-controller is locked.

To compare the lifetime of the red sheet-beam trap to the optical lattice trap, a similar experiment has to be conducted in the red sheet-beam trap. Recent data find a lifetime of approximately 1 minute for a BEC in the red sheet without the DMD-potential turned on. Experiments without the DMD-potential turned on cannot be conducted for the optical lattice trap, as due to its repulsive nature there is no horizontal confinement. As the DMD-potential may introduce photon scattering or other first-order collision processes, the BEC lifetime is affected by the DMD. The lifetime of both traps has to be compared with the DMD-potential turned on.

The lifetime data of the red sheet, taken shortly after the DMD was implemented, showed lifetimes which were highly dependent on the DMD power and a lifetime of 18.2 s was found to a DMD trap depth of 1.2μ [3]. The rapidly reducing lifetime by increasing the DMD potential was later found to be caused by presence of light when the DMD potential should have turned off. Unfortunately, no more recent data was taken on the lifetime in the red sheet trap before the system went offline, so it is challenging to quantitatively compare the BEC lifetime of both traps. Through day-to-day use, we observed a slightly longer lifetime in the red sheet-beam trap than the optical lattice trap at a DMD potential of $\sim 8\mu$. The measured lifetime of $\tau = 19(5)\,s$ is sufficiently long to perform the transport and turbulence experiments proposed in Chapter 6.

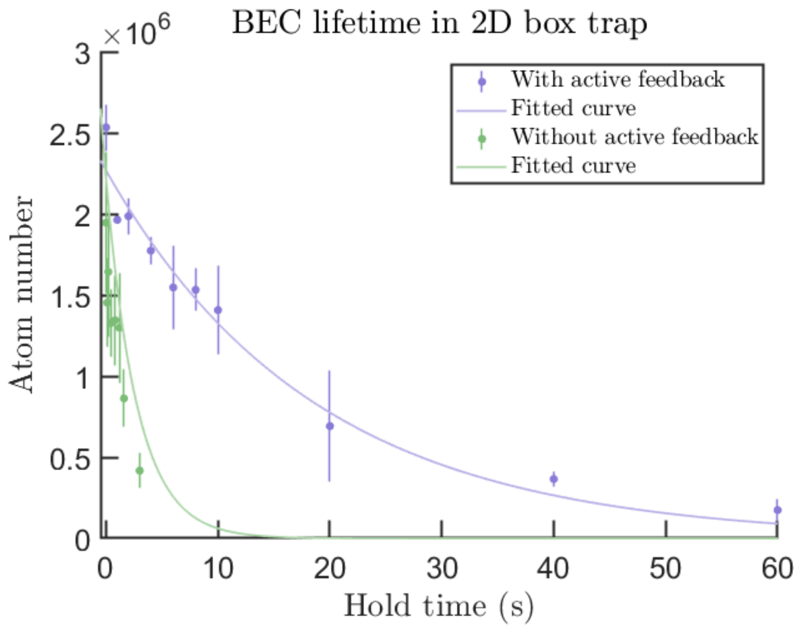

FIGURE 5.2: The atom number as a function of the time the trap held onto the atoms before measuring the atom number. The circles are experimental data, the solid lines are fitted curves based on Eq. 5.2. Purple and green represent measurements with, and without active feedback, respectively.

5.2 Trap frequency of the optical lattice

5.2.1 Background

Quantitative comparison of experiment to simulation or theory requires knowledge of the potentials used for trapping atoms. The trapping frequency of these potentials is a feature which greatly affects the dynamics of the system, as for instance, both the healing length and the speed of sound depend on it. Most optical dipole traps are approximated as harmonic oscillators, so to find the trap frequency of the optical lattice, the harmonic approximation must be applied. The trap frequency can then be computed by [32]:

$$\omega_i = \sqrt{\frac{1}{m_{Rb}} \partial_i^2 U_{\text{dip}}(\mathbf{r}=0)}\,, \qquad \nu_i = \frac{\omega_i}{2\pi} \qquad (i \in \{x, y, z\}), \tag{5.3}$$

where ω_i and ν_i the angular and linear frequency, m_{Rb} the mass of a Rubidium atom and ∂_i^2 the second derivative with $i \in \{x, y, z\}$.

This expression follows from the classic harmonic oscillator, $U_{\text{HO}}(x) = m\omega^2 x^2/2$. The Taylor series in Eq. 5.3 is taken to approximate a harmonic oscillator around $\mathbf{r} = 0$. U_{dip} is the potential of the optical dipole trap, given by Eq. 2.28.

Various experimental mechanisms can be used to determine the frequency of a trap. One of these methods is applying a short, pulse-like perturbation to the system. The horizontal and vertical waist of the cloud start to contract and expand, in an oscillatory manner called a breathing mode. The frequency of this oscillation corresponds to twice the trap frequency of the trap [33, 34]. Another method of determining the trap frequency of the system is currently being investigated at the University of Queensland by B. Mommers. In this method, the BEC is spatially, adiabatically oscillated. Through mapping of the trajectory of the cloud and analytically solving the GPE (Eq. 2.8) with a Husimi [35] driving term, the trap frequency can be determined.

The most common method of determining the trap frequency of optical or magnetic traps is through parametric heating [36, 37]. This method relies on the harmonicity of the trap, as this method approximates the trap as a harmonic oscillator using the harmonic approximation:

$$\hat{H} = \frac{\hat{p}^2}{2m_{\text{Rb}}} + \frac{1}{2} m_{\text{Rb}} \omega^2 \left[1 + \epsilon(t)\right] \hat{x}^2, \tag{5.4}$$

with $\epsilon(t)$ an applied perturbation.

From classical mechanics, it is well known that parametric resonance occurs when $\hat{x}(t) = x_0 \cos(\omega t)$ and $\epsilon(t) = \epsilon_0 \sin(2\omega t)$, i.e. at a driving frequency twice the resonance frequency. At this point, energy is pumped into the system at an exponential rate. The energy is transferred to the atoms which deplete from the trap as the trap depth is no longer deep enough to confine the now thermal atoms.

5.2.2 Modelling the optical lattice

The properties of the optical lattice can be predicted through modelling of the electric fields of both beams. Through use of Eq. 2.28, the trap depth, frequency, flatness and shape can be obtained for two interfering beams with given input power, waist and beam separation. For a beam input diameter of 2.67 mm and beam separation of 3.3 mm, the horizontal and vertical waist are 1120 μm and 25.4 μm, respectively. The lattice spacing is calculated using Eq. 4.1 and is found to be $\lambda_{\text{lattice}} = 32.2\,\mu$m for a beam separation of $d = 3.3$ mm. The corresponding potential and trap frequency uniformity for this waist and beam separation are shown in Figure 5.3. The centre trap frequency is expected to be $\nu_{\text{trap}} = 186$ Hz.

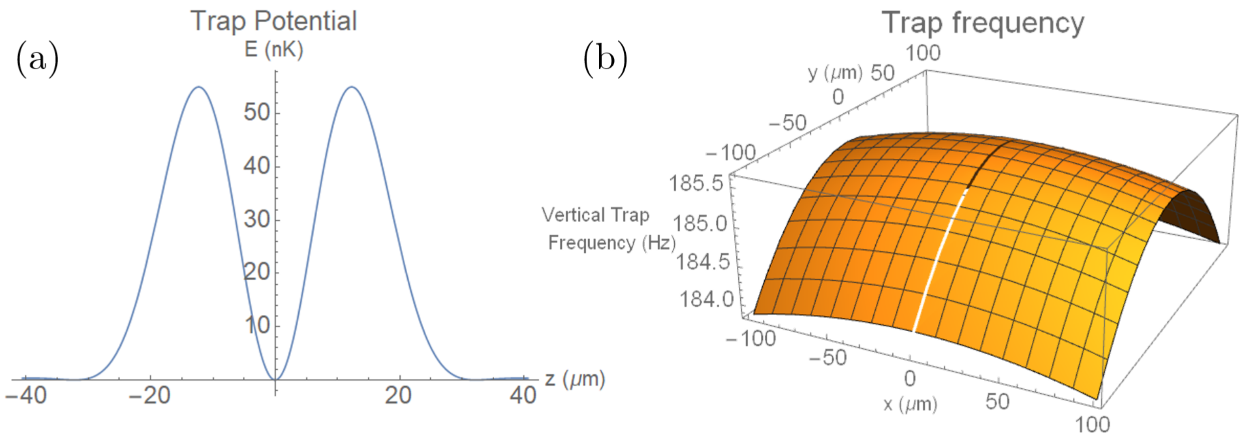

FIGURE 5.3: The simulated trap depth (a) and frequency (b). With the calculated vertical waist and beam separation, the lattice only consists of two fringes with a well in which the atoms are trapped in the centre. (b) shows the trap frequency throughout the trap. The large horizontal waist and Rayleigh length of the beam ensure a uniform potential, with variations of less than 0.5% throughout the DMD trap area.

5.2.3 Experimental Sequence

After transfer from the optical dipole trap to the red-detuned sheet trap, the DMD is ramped on. Similarly to the lifetime experiment, the imprinted potential used is a 50 μm radius circle. The red sheet trap power is ramped down at a similar rate as at which the optical lattice is ramped up for most efficient transfer. Once transferred to the optical lattice, the parametric heating process starts, in which the lattice is oscillated for 1 second. After oscillating, the atoms are held for an additional 500 ms before imaging to allow atoms to thermalize.

To find the parametric resonance, any periodic perturbation can be applied to the system. Because the active feedback is used in these experiments, fluctuating the intensity of the light through the AOM causes the feedback system to unlock, as we lock to a certain light intensity. By fluctuating the intensity, the PI-controller moves the mirror to find its locked-to power. The oscillating intensity, however, causes the integrator to overdrive which unlocks the controller, making periodically alternating the intensity to find the resonance

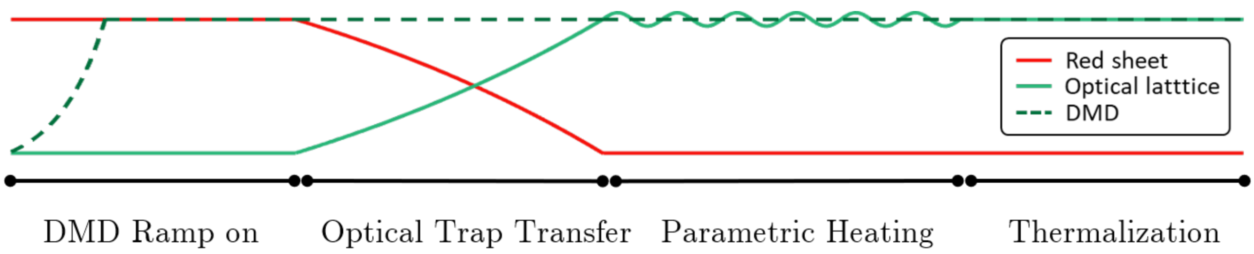

Figure 5.4: The experimental sequence for measuring the trap frequency of the optical lattice.

unreliable. The response time of the levitating magnetic field is too slow to apply periodic perturbations to the system using this method. In order to apply oscillations to the system, a periodic signal was applied to the input offset channel of the PI-controller. As a result, the lock-to value slightly oscillated, forcing the PI-controller to vibrate the fringes of the lattice in a controlled fashion: The system is perturbed by spatially oscillating the fringes.

5.2.4 Results and discussion

To get an estimation of the trap frequency, the measurements are performed within step sizes of 50 Hz. The amplitude of the oscillation is high, resulting in a broad resonance. This allows to scan over a large frequency range with a bigger step size, while still seeing the resonance. The disadvantage of a large amplitude is that all atoms will escape the trap around the resonance. It is challenging to find the centre frequency through fitting when

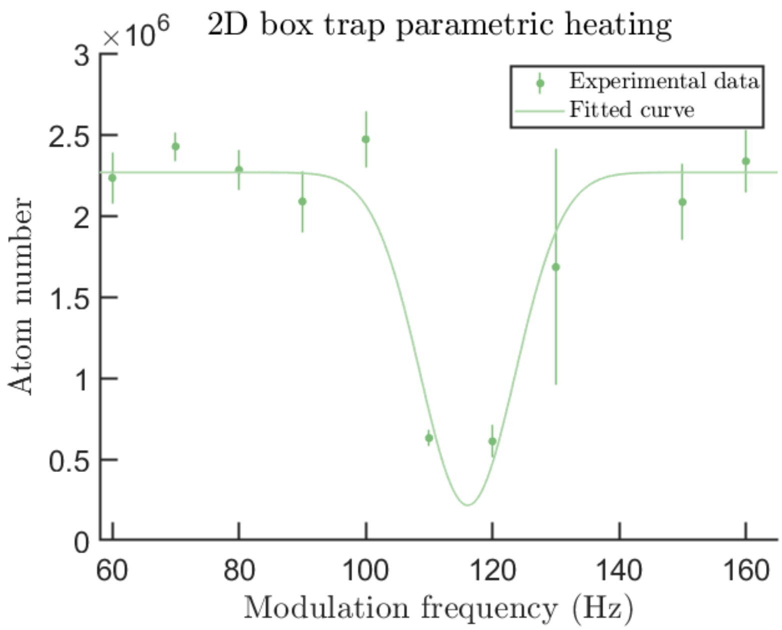

Figure 5.5: The atom number after oscillating the BEC for given frequencies. A clear dip is observed at twice the parametric resonance, i.e. twice the trap frequency.

at various frequencies, all atoms are expelled from the trap. As such, once the resonance is found, the measurement is repeated over a smaller frequency range and at a lower step size of 10 Hz. The amplitude is decreased to let a large portion, but not all the atoms escape. The data is then fitted using a Gaussian.

Far from resonance, the average atom number is found to be $N = 2.2 \cdot 10^6$. A clear dip is observed at a modulation frequency of $\nu_{\text{mod}} = 116(2)\,\text{Hz}$. The corresponding trap frequency, half the modulation frequency, is $\nu_{\text{trap}} = 58(1)\,\text{Hz}$, far from the predicted frequency of $\nu_{\text{trap}} = 186\,\text{Hz}$. The difference may be attributed to various factors: The beam separation may be different from the simulated one, the power at the atoms is lower than expected or the beam waists at the atoms is different from the calculated waists.

The vertical beam waists are not changed throughout the system, except for the final lens, which focusses the light on the atoms. As there are no lenses in the system that manipulate the beams vertically, the beam separation remains equal throughout the system. That allows us to measure the beam separation with high accuracy. The beam separation remains $d = 3.3\,\text{mm}$ and matches the simulated value.

The beam power is estimated by measuring the power before and after propagation through the Science Cell, which has uncoated windows. The power at the atoms is estimated by measuring the total beam power before and after propagation through the Science Cell. From that data, the power at the atoms is estimated by finding the transmission coefficient of the first window, which was found to be $T = 0.533$. Upon investigating the beam propagation throughout the system, we observed a slightly diffraction satellite beam coming out of the top beam. This satellite beam can be seen in the top beam before propagation throughout the Science Cell, but its presence becomes obvious far from propagation through the Cell. The presence of the satellite beam is expected to be a result from slightly misaligned optics in the tower. When the PBSs are not mounted perfectly, clipping may occur when the beams are close to the edge of the beamsplitters. When one of the cubes is not aligned with the other, a satellite beam may be formed in one of the beams which propagates through the system under a very small angle. As the satellite beam propagates under a slight angle, it will also be focussed on a slightly different spot; something we observed when aligning the lattice but was first considered to be an imaging artefact. It is challenging to measure the amount of power in this satellite beam and as such, to estimate the total power in the lattice. A lattice power lower than expected contributes to a lower trap frequency.

The waists for the beams at the atoms are calculated using a given exit diameter of the optical fibre after the AOM. After the fibre, the beam propagates through a series of cylindrical lenses which manipulate the horizontal beam waist, with the vertical waist only changed by the final lens, f_{final}. To investigate whether the actual beam waist matches the expected one, the beam waists are measured. The waists cannot directly be measured in situ through the camera of the BEC imaging system, as it is aligned to focus on 780 nm light. We can only get an estimation of the vertical waist based on the calculated lattice spacing for the known beam diameter using Eq. 4.1. Figure 5.6(a) depicts an image of the optical

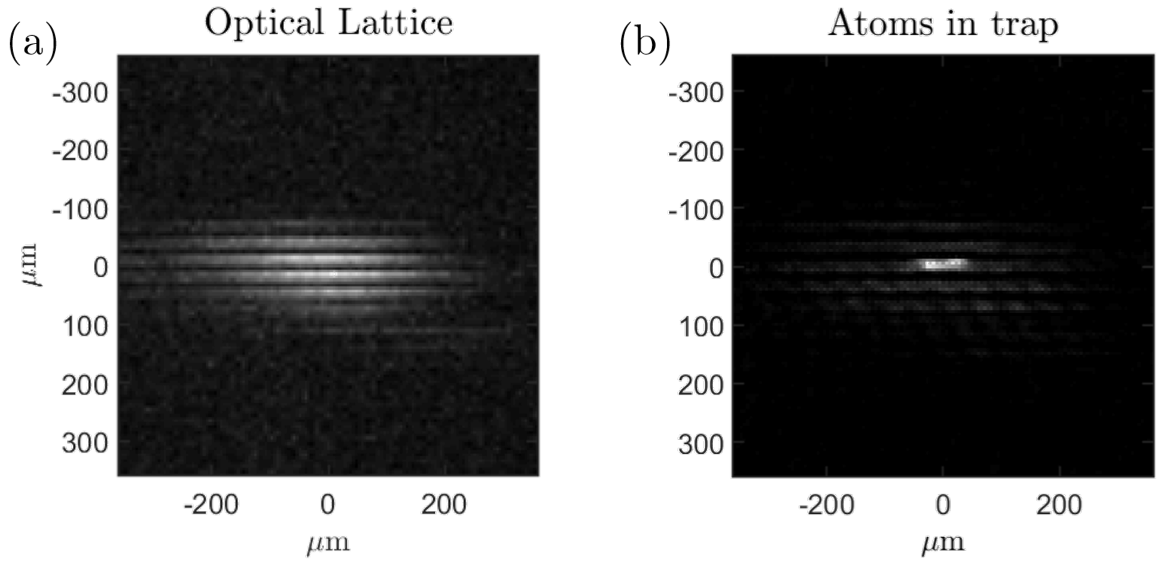

Figure 5.6: The optical lattice in situ, as imaged by the 780 nm imaging system. (a) depicts the lattice in situ. The dimensions on the axis do not correspond to the actual dimensions, as the imaged light is 532 nm, but the imaging system is set up for 780 nm light. As such, Fig. (a) is out of focus. We do observe more lattice nodes than expected and can therefore conclude the vertical waist must be larger than expected. To measure the vertical waist, a camera is mounted before the beams are focussed by f_{final}. Fig. (b) shows trapped atoms in situ. The image is taken using absorption imaging, i.e. with the 780 nm beam. The effective trap area is the size of the DMD-potential. The relatively small DMD-area compared to the lattice trap beam size ensures a large trap uniformity.

lattice in situ. The effective trap area can be seen in Fig. 5.6(b), which shows the atoms trapped in the lattice. As Fig. 5.6(a) is an image of a 532 nm beam on a system aligned for imaging 780 nm light, the dimensions on the axes don't match the actual beam size, as the image is out of focus. We can observe the vertical waist is bigger than expected, as more lattice nodes than expected are visible. To get accurate beam waist data, the waists have to be measured before f_{final}.

Upon measuring of the beam waists before f_{final}, a horizontal and vertical waist of $w_x = 1069(2)\,\mu$m and $w_z = 844(2)\,\mu$m are measured. After propagation through f_{final}, this results in a horizontal and vertical beam waist of $w_x = 1069(2)\,\mu$m and $w_z = 40.1(1)\,\mu$m at the atoms. While the horizontal beam waist is close to the expected value of $w_x = 1230\,\mu$m, the vertical waist, expected to be $w_z = 25.4\,\mu$m, is larger by almost a factor of two. This reduces the amount of power in the central fringes of the trap and as such, the trap frequency. The larger than expected vertical waist implies the beams are not perfectly collimated in the vertical direction, which over a long optical path have resulted in a slightly expanded beam.

The lower power in the top beam and the larger vertical beam waist contribute to a lower measured trap frequency than simulated. Future work on the optical lattice trap can overcome the power issue in the top beam through re-alignment of the optics in the non-common mode elements. Collimation of the vertical beam to match the beam waist at the atoms with the expected one is challenging, due to the divergence of Gaussian beams for small beam sizes: While initially a beam may appear collimated in a collimation device such as a shearing interferometer, over large distances, the beam may start to slightly diverge. To correct for a diverging beam, a slightly misaligned $1\times$ magnification telescope may be implemented into the setup far from the initially collimated point. The misalignment of this telescope can change a diverging wavefront to a collimated wavefront while approximately maintaining the same beam size.

6
Applications

Chapter 4 discussed the advantages of using a blue-detuned lattice trap over a red-detuned focussed beam trap. Since the lattice spacing can be adjusted by changing the beam separation, the trap potential isn't limited by Gaussian beam optics. The trap depth and frequency are easily adjusted and allow for trap frequencies in which the trapped BEC must be considered a quasi-two-dimensional condensate. The repulsive nature of the trap facilitates thermal atoms floating over the condensate to escape, which reduces noise on measurements. Finally, due to the large horizontal beam waist the trap is very uniform which opens the possibility of doing experiments on large area condensates without any density dependent forces acting on excitations like superfluid vortices.

This chapter proposes three experiments which can be executed with the new lattice trap, each of them utilizing a different feature of the trap. Section 6.1 discusses an experiment in which the large trap area is utilized in an experiment in which a superfluid analogue for the Reynolds number can be found. Section 6.2 proposes an experiment in which one of the features that classify a liquid as superfluid, called the fountain effect, can be measured utilizing the large trap depth and repulsive nature of the trap to remove extraneous thermal atoms. Finally, Section 6.3 proposes an experiment in which a bosonic version of 'quantized conductance' can be found. Quantized conductance has been observed for electrons (fermions) in 1988 using a two-dimensional electron gas and quantum point contacts. To find a quantized conductance for bosons, a 2D BEC is required. This experiment utilizes the ability to achieve trap frequencies high enough for the condensate to be considered fully two-dimensional.

6.1 Superfluid analogue to the Reynolds number

6.1.1 Introduction

One of the characteristic properties of superfluids is they flow without viscosity. Using the definition of the Reynolds number, used in classical fluid mechanics as a dimensionless quantity to characterize the degree of turbulence in a system, a singularity is reached when applying it on superfluids. Even though their inviscid behaviour, superfluids do exhibit dissipation and a clear distinction is seen between laminar and turbulent flow. The existence of dissipative excitations in superfluids which introduce turbulence, such as vortices, seem to suggest an analogous Reynolds number can be found for superfluids.

In classical fluids, wake turbulence is a common phenomenon in aviation. As the wing of an aircraft moves through air, vortex shedding occurs behind the wings. The same phenomenon occurs for water flowing past a buoy or landline phone wires signing in the wind. The irregularity of the shedding depends on the relative velocity of the fluid compared to the barrier. In 1878, Czech physicist Vincec Strouhal experimented with vortex shedding in phone wires singing in the wind [38]. Strouhal found the frequency of the vortex shedding was related to the thickness of the wire – the characteristic length scale – and the flow velocity. The three parameters are expressed in the dimensionless Strouhal number

$$\mathrm{Sr} = \frac{fD}{u}, \tag{6.1}$$

with f the frequency of the shedding, D the characteristic length scale and u the relative velocity of the fluid to the obstacle.

Because of the dynamical similarity between the Strouhal number and the Reynolds number $\mathrm{Re} = uD/\nu$ (with ν the kinematic viscosity), the Strouhal number is a universal function for the Reynolds number. As vortex shedding is a phenomenon which occurs in both classical fluids and superfluids, a superfluid analogue of the Reynolds number can be defined and tested as a function of the Strouhal number. As noted, although there is no viscosity in superfluids, energy dissipation occurs through vortices. Moreover, the quantum of circulation h/m (as discussed in Sec. 2.1.3) has the same units as viscosity, as first noted by Onsager in 1953 [39].

Plotting St against a superfluid Reynolds number defined as

$$\mathrm{Re}_s \equiv \frac{(u - u_c)D}{\kappa}, \tag{6.2}$$

with u_c the critical velocity in the superfluid and $\kappa \equiv \hbar/m$[1], reveals dynamical similarity of the classical and the quantum cylinder wake. [40]

[1]Note that, contrary to the definition in Chapter 2, κ is here defined as $\kappa \equiv \hbar/m$ because this results in a transition from laminar to turbulent flow near $\mathrm{Re}_s \sim 1$.

6.1.2 Previous experimental studies

Numerical studies of this phenomenon have been conducted by M. Reeves [18], by simulating a BEC flowing past a circular barrier. For obstacle sizes larger than a few healing lengths, a von Kármán vortex street is formed which exhibits a universal St-Re$_s$ relation similar to the classical one. Upon decreasing the barrier size, a new quantum regime is observed. Although experimental studies have observed the von Kármán vortex street, [41], the regimes from the numerical study aren't clearly observed and transition to turbulence doesn't quite match the prediction. To achieve the wake in an experimental setting, a barrier is swept through the stationary condensate. Since the vorticity at the boundaries of the superfluid is zero, a large condensate is required for any vortex shedding to occur. In addition to a large condensate, it is essential to have a uniform trap, so the superfluid critical velocity is uniform along the barrier path and furthermore, so there is no density dependent force gradient acting on the vortices.

A previous experimental attempt to perform this study using the red-detuned sheet trap was restricted to using a smaller condensate area due to trap non-uniformity. Figure 6.1 shows a comparison between atoms loaded in the optical lattice trap and red-sheet trap. In the optical lattice image, atoms are loaded into a rectangle almost the size of the DMD beam which confines the atoms horizontally and prints patterns into the BEC. The image on the right shows a density image of the rectangle used for the earlier superfluid Reynolds experiment. The area into which the atoms are loaded is smaller, but with the largest area to uniformity possible within the red sheet trap. Note that the scale of both images is the same.

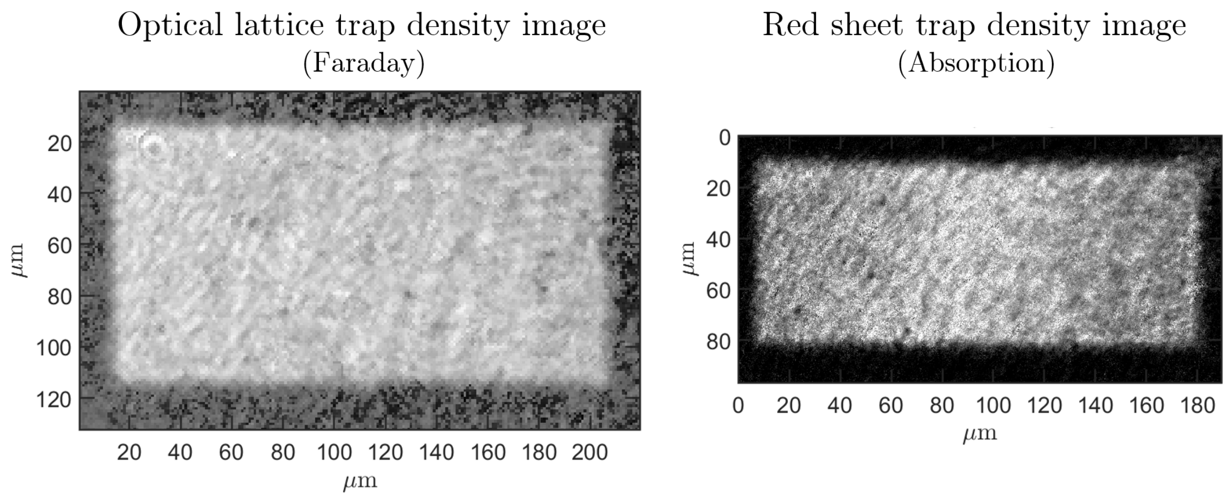

Figure 6.1: A comparison between the area which could be used for the superfluid Reynolds number experiment in the optical lattice trap versus the largest area in the red sheet trap, used in a previous attempt to perform this experiment at UQ.

Unfortunately, due to the different mechanisms used for imaging in both experiments, it is not possible to quantitatively compare both traps. The image in the optical lattice is made using phase-contrast Faraday imaging (see Sec. 3.3 whereas the red-sheet trap image is made using absorption imaging. Both images have been processed to be linearly proportional to the atomic density, $n(\mathbf{r})$, however the Faraday image could not be directly scaled to $n(\mathbf{r})$ because the background light intensity was not measured before the system went offline. Due to the absence of proper scaling, the density image of the optical lattice is expressed in $\phi(\mathbf{r})$ ($\phi(\mathbf{r}) \propto n(\mathbf{r})$, see Eq. 3.1 and 3.2) which is why the background looks much more noisy than the red-sheet image. Qualitatively, however, it is obvious the trap area in the optical lattice is much larger, while still uniform. The red sheet trap can be increased to the same size, but the non-uniformity of the trap would be too great to perform experiments. The density peak in the centre of the red sheet not only introduces a force gradient acting on the vortices, it also results in a variation of the critical superfluid velocity (Eq. 6.2), which introduces additional challenges in finding the superfluid Reynold's number.

6.1.3 Proposed experiment

Experimental observation of the three vortex shedding regimes and the transition to turbulence using equation 6.2 can be done through preparation of a sequence of images uploaded to the DMD which sweep a barrier through the superfluid. The barrier speed and size are varied to observe the three regimes, the oblique dipole (OD), the charge-2 von Kármán and irregular shedding, as shown in Fig. 6.2. At low Re_s, vortex dipoles are released obliquely from the barrier (OD). As Re_s is increased, a charge-2 von Kármán vortex street appears (K2). The Strouhal number has a maximum around and drops after $\mathrm{Re}_s \sim 0.7$. Beyond this value, vortex shedding becomes irregular, which is a clear indication of turbulence. For semi-classical barriers, in which the barrier size is considerably larger than the healing length, the OD regime is missing, which is also the case in classical fluids.

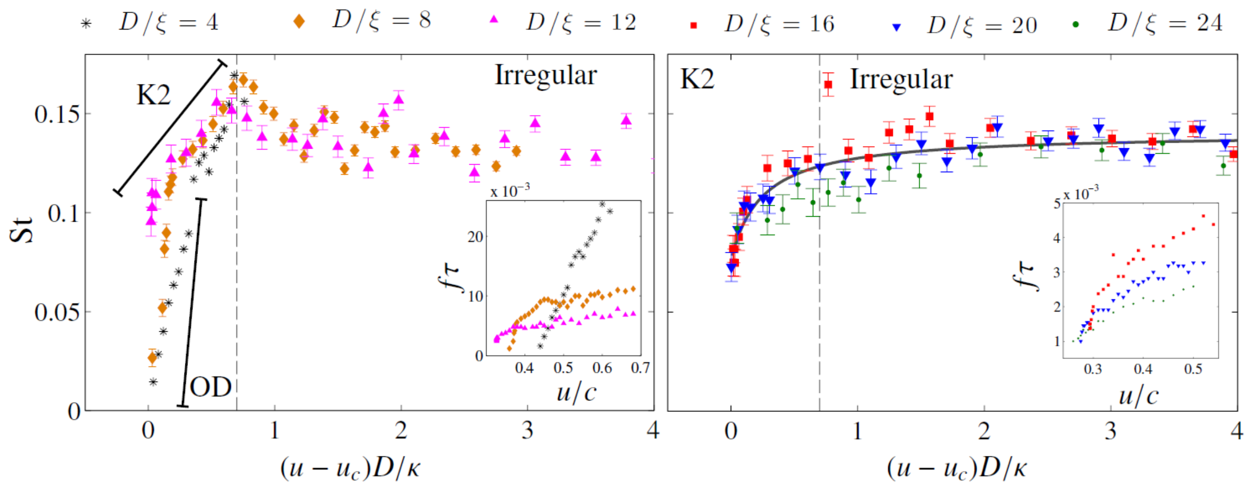

FIGURE 6.2: Strouhal number as a function of the superfluid Reynolds number. The figure on the left shows the three regimes visible when the barrier size is comparatively small to the healing length, the quantum barrier. The image on the right shows the Strouhal number as a function of Re_s for larger barrier sizes, the semi-classical case. In this case, the oblique dipole (OD) regime is clearly missing. Retrieved from "Identifying a Superfluid Reynolds Number via Dynamical Similarity", M.T. Reeves et al., *Phys. Rev. Lett.* **114**, 155302 [18].

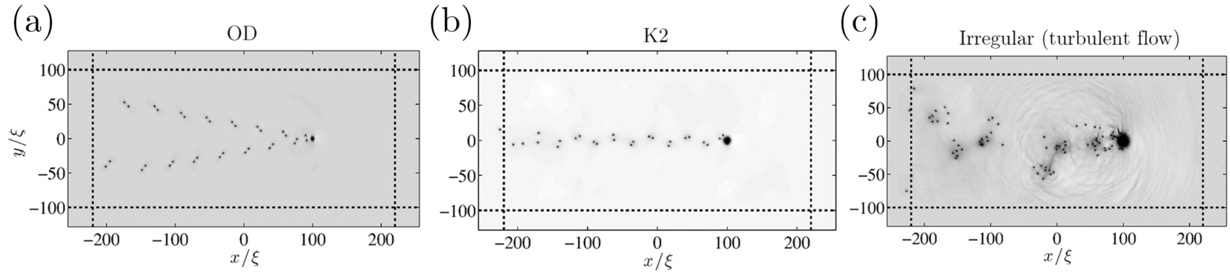

Figure 6.3: The three different regimes in the von Kármán vortex street. (a) shows oblique dipole shedding, in which dipole are obliquely released from the barrier, (b) shows the charge-2 von Kármán shedding, in which charge-2 von Kármán vortex street appears and (c) shows irregular shedding, which indicates turbulent flow. Adapted from "Identifying a Superfluid Reynolds Number via Dynamical Similarity", M.T. Reeves et al., *Phys. Rev. Lett.* **114**, 155302 [18].

Although a circular barrier is used in the numerical study, a square barrier has a much higher drag coefficient. At higher drag coefficients, a lower relative velocity is required in order to see the different regimes. In previous studies it was hard to find the OD regime and it might therefore be favourable to use a square barrier at lower velocities to see oblique shedding appear before the barrier exits the condensate. To further help break the initial symmetry in the superfluid, which prevents vortices from forming, it is useful to slightly angle the plane of incidence. Numerical simulations in which experimental limitations were considered, conducted by T. Bell at UQ [42] found that using an incident plane with an inclination of 56° maximises the street length.

To find the Strouhal and superfluid Reynolds number from the experimental data, the wake velocity must be calculated. Direct wake velocity measurements would require non-destructive imaging techniques or could alternatively be calculated using the vortex' signs. This method would generally require Bragg diffraction signed vortex detection methods [43]. However, in the von Kármán vortex street regime, vortices are shedded sufficiently regular that the vortex signs can be determined by looking at the vortex position and propagation alone.

6.2 Superfluid fountain effect

6.2.1 Introduction

Superfluidity was first realised in liquid ^{4}He in 1938 when it was cooled below a critical temperature [44]. Shortly after first realisation of superfluidity, the superfluid fountain effect was observed [45]. Allen et al. observed ^{4}He flow from a cold to hot channel. It was not until 1941 that Landau proposed the two-fluid model [46] which was able to explain the counter intuitive flow, which appeared to violate the second law of thermodynamics. While one of the first effects discovered in superfluid Helium, and in fact one of the characteristic traits of superfluidity, the fountain effect has not yet been observed in a BEC.

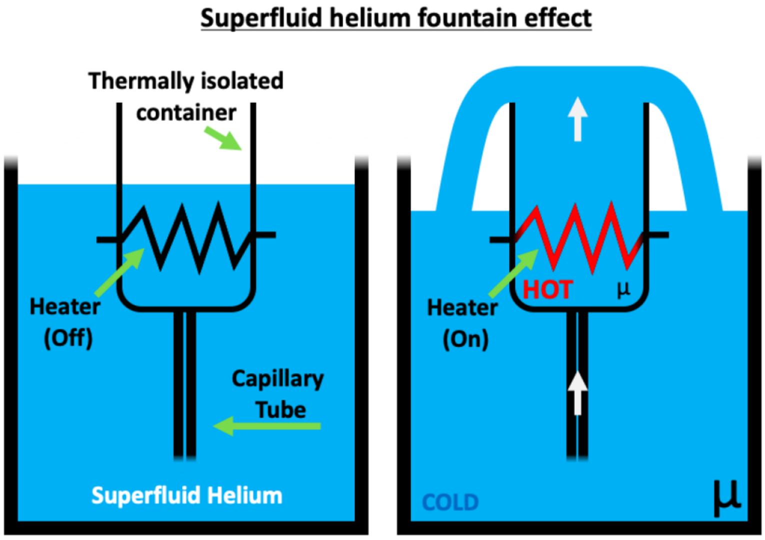

FIGURE 6.4: The superfluid helium fountain effect. The image on the left shows the system in thermal equilibrium. The system consists of a large reservoir and a smaller thermally isolated container connected by a superleak, depicted by a capillary. The image on the right shows the system after heating the container. The heating induces a difference in chemical potential (μ), which is higher for the cold reservoir. As such, superfluid helium flows from the smaller to larger chemical potential. Adapted from "Looking for the Superfluid Fountain Effect in a Bose-Einstein Condensate", C. Manning, University of Queensland [47].

Landau's two-fluid model described a superfluid as composing of two components: A viscous, 'normal' part, which transports heat (or entropy) and a superfluid part which flows without viscosity and cannot transport heat. In the superfluid helium fountain effect, two reservoirs are thermally isolated from each other and connected by a superleak, depicted in Fig. 6.4 as a capillary tube. The superleak is too small for the viscous fluid to flow through because of its surface tension. The superfluid part of the two-fluid model fluid can, however, flow between both reservoirs, because it has zero viscosity.

One of the reservoirs is heated up and the system is now out of thermal equilibrium. The difference in temperature consequently means there is a difference between chemical potential between the reservoirs with a gradient pointing into the opposite direction of the temperature gradient. The imbalance in chemical potential leaves the system out of mechanical balance and fluid starts overflowing from one reservoir to the other, much like a fountain. As only the normal part of the fluid can transport heat and the superleak prevents the normal part from flowing back into the hot channel, the superfluid and normal fluid start to separate as the system tries to get back into equilibrium.

While other characteristics of superfluidity, such as non-dissipative fluid flow and formations of quantized vortices have been observed in superfluid BECs, the fountain effect has yet to be observed. Utilizing the high trap depth of the optical lattice trap, thermal atoms can be trapped to conduct the superfluid fountain effect experiment.

6.2.2 Previous experimental studies

A previous experimental study to the superfluid fountain effect in BECs was conducted at the UQ BEC lab in 2015. The two reservoirs were created in a 2D dumbbell shape using the DMD. Initially the reservoirs are not connected, and one is larger than the other. After loading the atoms into the shape, the reservoir is shrunk and stirred, which heats up the reservoir. A short time built into the sequence to allow any sound waves or other excitations to leave the superfluid. At this point, the reservoirs are connected through a narrow channel. The channel width is small enough to allow only superfluid transport from the cold to hot reservoir. A bimodal analysis of the atoms, which allows to fit the number of thermal atoms and the number of atoms in the condensate using the Thomas-Fermi approximation can only be performed for one channel at the time. As such, after transport, one of the channels is illuminated with resonant light. The atoms in the illuminated reservoir are excited and escape the trap, leaving only the other channel for analysis. The measurement is then repeated to analyse the other channel.

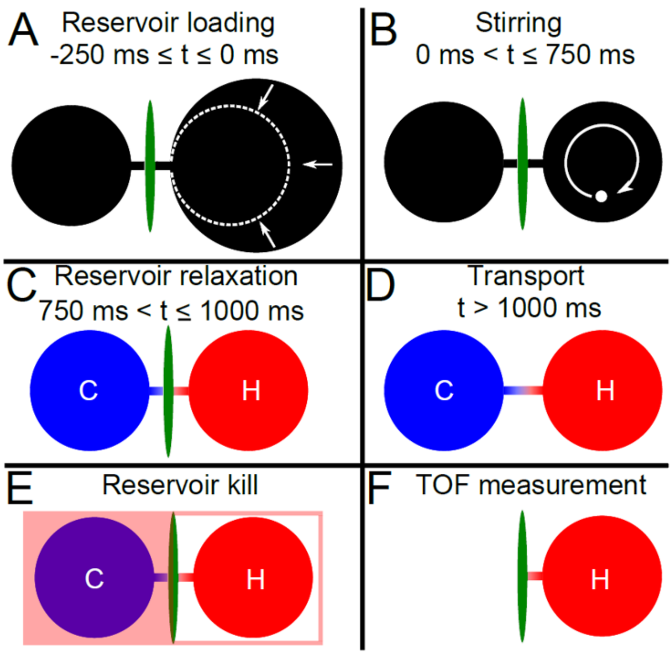

Figure 6.5: The experimental sequence of the previous experimental study to the superfluid fountain effect. Two reservoirs are formed, one of which initially larger than the other. After shrinking and stirring of one reservoir, both channels are out of thermal equilibrium. At this point, the reservoirs are connected by a narrow channel to allow transport. At this point, the fountain effect should take place in which atoms flow from the cold to the hot reservoir. As analysis is only performed one channel at a time, resonant light is used to excite the atoms in one of the reservoir channels. Image provided by Guillaume Gauthier.

The experimental study was inconclusive due to various issues with the used experimental setup and methods used at that time. The largest issue with the setup at that time was due to the attractive nature of the red-sheet trap. Atoms were still trapped in the sheet trap but were not trapped in the DMD trap (due to a too low trap depth of this trap), which may have the two reservoirs in thermal contact at and for an unknown time. This poses an issue as this may have allowed transport between the reservoirs without the channel. As such very little change was observed upon measuring the relative condensate fractions in both channels after different times. The possibility of floating of atoms outside the DMD potential is eliminated when using the optical lattice trap, as atoms floating outside of the trap experience a force gradient which moves away the atoms away from the trap. Furthermore, during the realisation of the optical lattice trap, the trap depth of the DMD was increased by replacing the optical fibres in the setup to fibres which couple light better, resulting in a higher overall power in the DMD optical path.

6.2.3 Proposed experiment

In a new proposed experiment at UQ, a study if performed to finding the superfluid fountain effect in a BEC using the optical lattice trap and improved DMD trap to have sufficient trap depth. If the trap depths in both traps are deep enough to trap thermal atoms, the study can be conducted. The repulsive nature of the optical lattice trap ensures that if any atoms are not trapped by the DMD potential, these atoms are expelled from the trap.

In the new proposed study, another method of heating one of the channels is used. This new method is used to ensure the temperature gradient between both reservoirs is sufficiently high. Step (a) in Figure 6.5 is omitted and instead the BEC is heated through a 'bubbling' method, developed by C. Manning [47]. In this method, DMD mirrors are quickly turned on and off on one of the channels. When done at the right frequency, this pumps energy in the system which results in heating of atoms.

While the first stages of finding the superfluid fountain effect in the new trap were performed by C. Manning, the experimental study is still an ongoing investigation. Upon the first attempts to find the effect, the optical lattice trap depth was not sufficiently high yet. Better coupling in the optical fibre in the future and better alignment in the components in the tower of the setup (see Fig. 4.3) should give a sufficient trap depth according to our simulations. To use this in experiments, the PI-controller in the active feedback system must be configured accordingly to be able to function at these higher powers. Current limitations to measuring the fountain effect are due to solving these engineering problems. These problems could not be solved, however, before the system went offline. Once the system is online again, the experimental study can be continued.

6.3 Quantized conductance of bosons

6.3.1 Introduction

Quantized conductance was first observed in 1988 independently by researchers at Cambridge University [48], as well as by researchers at Philips Laboratory and the University of Delft [49]. First observed in a quantum point contact, it was found that increasing the voltage over the contact only increases the current in discrete steps, quantizing the conductance in steps of $\frac{\pi e^2}{\hbar}$. Quantized conductance has been shown to be a useful tool in atomic switches [50], and Conductive Bridge Random Access Memory (CBRAM) [51], steadily making its way to consumer products [52].

Although being a well-established phenomenon for fermions, other than theoretical predictions of a similar phenomenon existing for bosonic transport [53], so far no experimental proof has been provided. The creation of a one-dimensional channel between two reservoirs, a setup similar to the superfluid fountain experiment, allows two investigate transport from one to the other reservoir. If the channel is sufficiently small enough to be considered a 1D channel, and the chemical potential difference between both reservoirs is sufficiently high, quantized conductance for bosons can be measured.

6.3.2 Previous and proposed experimental studies

To perform this experiment in a BEC, a geometry of two reservoirs is created, connected by a small channel, similar to Fig. 6.5. To observe quantized conductance, it is crucial the two reservoirs are thermally insulated and the channel's width and height are small enough to only allow 1D transport.

A previous study conducted at UQ investigated transport for channels with small width. In this investigation, the red sheet-beam trap was utilized. Because of its low vertical trap frequency, the channel still had to be considered 2D. Moreover, because of the attractive nature of the red sheet-beam trap, thermal atoms were floating around the pattern. An effect first described by Ketterle's group, called distillation [54] allowed transport between both reservoirs, even in absence of a channel. Due to a difference in trap depth of both channels (necessary for transport to occur), atoms are transported from the 'hotter' to the 'colder' channel. This transport is facilitated by the thermal cloud, which couples both channels. The atoms can condense again in the colder channel, much like classical distillation.

The optical lattice trap overcomes both issues simultaneously: Because of its repulsive nature, thermal atoms are expelled from the trap, thus getting rid of any distillation to occur. The ability to increase the trap frequency by reducing the lattice spacing will allow one to create a true 1D channel to connect both reservoirs and observe quantized conductance.

7 Conclusion

Red-detuned ODTs are a great tool for trapping BECs. When vertically focussed to a tight beam, red-detuned ODTs provide sufficient confinement for a great range of 2D BEC experiments [6, 7]. The current red-sheet beam trap in the BEC experiment at UQ, however has a limited trap depth and frequency. Moreover, as it is a focussed Gaussian beam, the vertical beam waist is always limited to the Rayleigh range of the beam. In other words, higher trap frequencies cause lower trap uniformity. As a non-uniform trap introduces a force gradient on the atoms, these are undesired features in superfluid experiments. In this thesis, a new trap is proposed and realized which allows to execute experiments at much higher trap frequencies with much improved trap uniformity.

The proposed trap is realised by trapping atoms in node of a blue-detuned optical lattice. The optical lattice is created through interference of two identical 532 nm beams, created using two PBS cubes. Through control of the intensity of the light using AOMs and the lattice spacing by changing the beam separation, the trap frequency can be adjusted over a large range. Through the use of an active feedback system, the vibrations of the lattice are removed to achieve long BEC lifetimes in the trap.

At the time the optical lattice was realised in the experiment at UQ, the measured trap frequency was found to be $\nu_{\text{trap}} = 58(1)\,\text{Hz}$. This is much lower than the trap frequency expected from the performed simulation, which was $\nu_{\text{sim}} = 186\,\text{Hz}$. Upon investigating the difference between the simulated and experimental frequency, the measured beam waists near the atoms did not match the calculated and simulated ones. This might be due to slight misalignments in telescopes in the setup. The setup is relatively long and as such a slightly diverging beam can significantly change the beam waist on a focussed spot. In addition, the power in the lattice at the atoms might have been lower than expected. Due to clipping of a very small part of the beam on one of the PBSs, a satellite beam was created far from the PBS and close to the atoms. This reduced the actual optical power in the lattice, and therefore the trap frequency.

The 1/e BEC lifetime in the trap was found to be $\tau = 19(5)\,\mathrm{s}$, which is of the same order of the red-sheet beam when the DMD potential was first implemented [3] and is sufficient for superfluid transport and turbulence experiments. To achieve this lifetime, an active feedback system had to be implemented in the system, which allowed to lock the relative phase between both beams using a PI-controller. The feedback system compensates for any vibrations near the trap frequency, which heats the atoms and allows them to escape the trap. Without using an active feedback system, the BEC lifetime was found to be $\tau = 2.8(8)\,\mathrm{s}$. While the feedback system currently does not operate at higher laser powers, it is a simple matter of engineering to overcome this limitation.

Before work could start to re-align the optics in order to have the desired beam waist size at the atoms and remove the clipping at the PBS, the experiment went offline due to a leak in the vacuum. As soon as the system is back online, work can start to improve the setup. An example of a feature which could be implemented is a $1\times$ magnification telescope close to the atoms, to compensate for any beam divergence in the system and have a less curved wavefront incident on the lens which focusses the light to form the optical lattice.

The new trap opens a range of new experiments. Three of these experiments were discussed in the thesis: A superfluid Reynolds number analogue, the superfluid fountain effect in a BEC and quantized conductance for bosons. The superfluid Reynolds number experiment can be executed as soon as the experiment is back online, as it only requires low trap frequencies but utilizes the high trap uniformity of the setup. The superfluid fountain effect in BECs experiment can be performed as soon as a sufficient amount of power can be coupled in the trap, as this experiment involves trapping of thermal (not-condensed) atoms. After re-alignment of the optics, this experiment can be executed. After further improvements of the optical lattice, such as implementation of the ability to actively change the fringe spacing when the atoms are loaded in the trap, the proposed quantized conductance for bosons experiment can be performed, for which a quasi-2D BEC is not sufficient. Using the high power and small lattice spacing, the setup should theoretically be able to reach trap frequencies sufficient to confine a BEC completely two-dimensional.

A

A detailed look at the optical lattice setup

In Chapter 4, a summary was given on components the optical lattice setup. The summary describes the setup sufficiently well to understand the setup without being too heavy on the details. In this Appendix, a more detailed description of all components in the setup is given, with sufficient detail such that the setup may be reproduced. Section A.1 lists every component and its function in the setup and in Section A.2, we briefly touch upon the effects of thermal lensing in setups when working with high intensity laser beams. A method is described to effectively cancel thermal lensing effects in AOMs. This method, proposed by Simonelli et al. [55], is tested and the advantages and disadvantages of using this method are discussed.

A.1 A walk-through of all components

The following section provides a list of all components used in the optical lattice setup with provided description. Numbers in the list correspond with labels in Figure A.1 and A.2.

1. A telescope consisting of a -25 mm and a 100 mm lens to initially expand the laser beam. Because of the small laser size, the -25 mm lens is an aspheric lens, to prevent spherical aberrations. The laser light coming out of the laser is $P_{\text{laser}} = 10\,\text{W}$ at $\lambda_{\text{light}} = 532\,\text{nm}$.

2. A high power polarizing beamsplitter with $\lambda/2$ waveplate mounted in front of the PBS. The waveplate sets the polarisation to be 70/30 horizontal/vertical. This means 7 W of laser power is being reflected onto the optical lattice path and 3 W is being transmitted to the DMD potential path.

3. The DMD-potential path. During this project, a new fibre was implemented in the

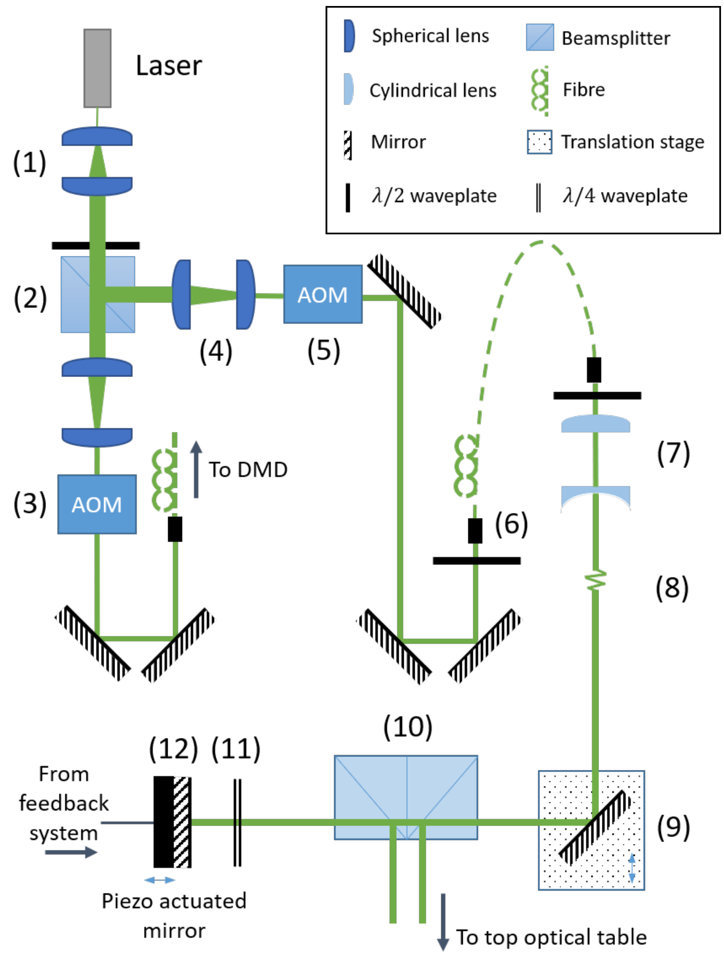

FIGURE A.1: A diagram of all optical components found on the lower optical table, identical to Fig. 4.2, with added labels.

system to increase the transmitted power and as such, the trap depth of the DMD-potential. The path from (2) to the DMD fibre is identical to the optical lattice path.

4. A 150 mm and -50 mm telescope, to reduce the beam size to the aperture of the AOM. Two telescopes are used to first expand and then reduce the beam size, as no aspheric lens of the right focal length was available to change the beam size to the right aperture using a single telescope.

5. A dense flint-glass B-coated AOM. This AOM sets the power distributed to the optical lattice. The zeroth order is used to dump excess light onto a beam dump. Over the course of this project, this AOM was changed from a tellurium dioxide (TeO_2) A-coated AOM to a dense flint-glass B-coated AOM. It was found that (TeO_2) suffers greatly from a thermal lens when used for high intensity applications. This resulted in a very non-Gaussian beam profile which spatially moved when the power was changed in the path. Consequently, the beam quality at the optical lattice was poor and the lattice

moved when the AOM was heating up. Section A.2 discusses this issue in more detail. The TeO_2 was changed with a dense flint-glass crystal AOM, which was only available with a B-coating (used for infrared applications) at the time of implementation. As such, the total efficiency of the AOM is only approximately $\sim 60\%$.

6. A fibre is used to decouple parts (1-5) from the rest of the setup and to spatially filter the light. If any of the optics are misaligned or changed (for example when changing to an A-coated quartz AOM), the optical lattice will still be aligned. Moreover, the fibre couplers act as spatial filters, as even though almost no thermal lens will be present in the quartz AOM, there are still some aberrations on the wavefront. The beam which has propagated through the fibre will have an (almost) perfect Gaussian wavefront again. The fibres used are polarisation maintaining fibres. To maintain the polarisation of the beam through the fibre, the incident polarisation must be aligned with the birefringence axis (see Sec 4.4 for more details). As such, a $\lambda/2$ waveplate is present before and after the fibre: The waveplate in front of the fibre is there to align the polarisation with the birefringence axis and the waveplate after the fibre sets the right polarisation to split the beam in equal powers at (10).

7. The beam waist after the fibre coupler is 1.34 mm, to prevent any other thermal lensing effects in the setup, the intensity of the beam is reduced by expanding in the horizontal beam waist to 4.0 mm using a series of -50 and 150 mm cylindrical lenses. The waist is only expanded in the horizontal direction to allow the beams to be reflected very close to the edge of the PBSs at (10), which allows us to have a small beam separation and as such, have a large lattice spacing (see Eq. 4.1).

8. The discontinuity of the line here represents a change of axis. The next components are mounted on the tower, which are mounted in the z-direction.

9. The light is reflected onto the PBS at (10) using a mirror mounted on a translation stage. The translation stage can move in such a manner that it deflects the beam further and closer to the edge of the PBS. As such, this mirror sets the beam separation.

10. The two PBSs split the beam into two. To obtain an optical lattice with zero intensity at the nodes (i.e. a high fringe fidelity), the power in both beams must be the same. To achieve this, the $\lambda/2$ waveplate at (7) sets the polarisation to 50/50. This reflects the vertically polarised light on the first and transmits the horizontally polarised light on both the first and the second PBS.

11. The transmitted light is reflected by a mirror at (12), to reflect this light on the second PBS, the polarisation must rotated vertically. This is done by the $\lambda/4$ waveplate. As the beam travels through the waveplate twice, a $\lambda/4$ is used.

12. A mirror mounted on a piezoelectric actuator reflects the beam such that it can be reflected by the second beamsplitter. The piezoelectric actuator is part of the feedback system which stabilizes shaking of the lattice at the atoms. By measuring a signal at

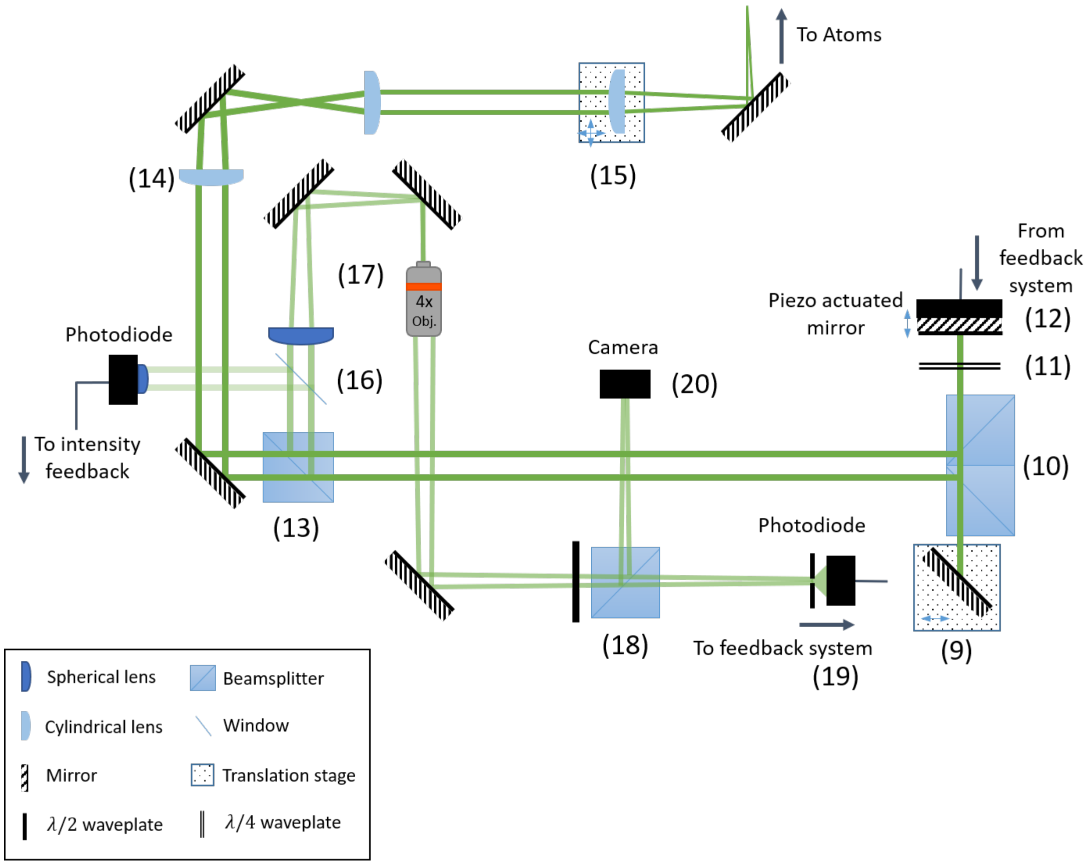

FIGURE A.2: A diagram of all optical components found on the top optical table, identical to Fig. 4.3, with added labels.

(19) and comparing this to the locked-on signal value, the PI-controller sends the error signal to the piezo at (12) to move the measured signal back to the locked-on signal. A more detailed description of the feedback system can be found in Section 4.3.

13. As the light is polarised in the vertical direction, almost all the light at the PBS at (13) is transmitted. A small fraction of the light is reflected due to the finite extinction ratio of the beamsplitter. This light is used for the feedback system.

14. The transmitted light at (13) goes to the atoms. At (14) the horizontal waist is reduced again to increase the intensity of the beam. A 250 mm and 70 mm cylindrical lens are used to reduce the horizontal beam waist to $w_x = 1.12\,\mathrm{mm}$.

15. The final cylindrical lens, $f_{\mathrm{final}} = 200\,\mathrm{mm}$ focusses the beams vertically, such that an interference pattern is formed at the atoms. This lens is mounted on a series of translation mounts, to ensure the lens is aligned with the optical axis. Misalignment in the optical axis results in the beams interfering on an angle. As a result, the atoms will fall out on the side. To prevent this, the lens is mounted on a rotation stage which also allows the lens to move in the x, y and z direction.

16. A glass window, mounted under a 45° angle is mounted in the feedback path. The small fraction of reflected light is refracted on the photodiode connected to the AOM at (5) to control the intensity in the optical lattice. When the diode detects too much power, the AOM sends more power through the zeroth diffraction order, which is dumped into a beam dump. The amount of power in the optical lattice path during the sequence is controlled by an experimental sequence programme, developed for cold-atom experiments, called Cicero.

17. The light transmitted through the window is focussed by a lens and another series of lenses (a 4× magnification finite conjugated objective is used for this). The objective is aligned so that it is part of an imperfect or slightly misaligned telescope. As a result, all lenses combined act as a single lens with a long focal distance, a telephoto. The focal distance of the combined lenses is approximately $f_{\text{telephoto}} \approx 550\,\text{mm}$ The long focal distance ensures a large enough fringe spacing to work efficiently for the feedback system.

18. The light is split again using a PBS and a $\lambda/2$ waveplate. The majority of the light is transmitted to the photodiode at (19) and a small fraction is sent to the camera at (20).

19. A $45\,\mu$m pinhole is mounted at the point in which the two beams interfere. The focal distance of $f_{\text{telephoto}} \approx 550\,\text{mm}$ results in a fringe spacing of approximately $\lambda_{\text{lattice}} \approx 90\,\mu$m, which is sufficiently large for the pinhole to sample a small portion of the beam. This small portion of the beam is detected by the photodetector, mounted next to the pinhole. The photodetector translates the intensity of the light diffracted by the pinhole to a voltage, supplied to the PI-controller. This photodetector is the input signal on the PI-controller. Section 4.3 discusses the feedback system in more detail.

20. A camera is mounted at the focal point of the telephoto to monitor the stability of the optical lattice. As the lenses used in the telephoto do not have the same focal distance as f_{final}, this camera cannot be used to measure the fringe spacing and the waist of the beam at the atoms. The frame rate of the camera is sufficiently high to monitor low frequent vibrations in the lattice.

A.2 Thermal lensing in AOMs

A.2.1 Introduction

A common occurrence in optical setups that operate with high intensity lasers is thermal lensing. This occurs upon transmission of high intensity laser beams through optical components with a sufficiently high absorption coefficient. The absorbed light heats up the optical component which induces mechanical stress and furthermore changes the refractive index of the material, which always features some temperature dependence. As such, the material locally deforms and has an altered index of refraction, which introduces aberrations in the wavefront. Upon propagating through these materials, a collimated wavefront may obtain a small focus, or the quality of the wavefront can decrease.

In many cases, one may choose to use optical components of a different material to prevent thermal lensing. UV Fused Silica (UVFS), for example, has a much lower absorbance than the commonly used N-BK7 [56]. In some cases, however, changing optical components is not a feasible option and alternative methods have to be found in order to minimize the amount of thermal lensing in an optical setup.

In the setup at UQ, tellurium dioxide (TeO_2) crystal AOMs were used for controlling the intensity of the $\lambda_{\text{light}} = 532\,\text{nm}$ DMD-potential and the optical lattice. These AOMs were chosen because of their high diffraction efficiency for visible light. The optical lattice was implemented over the course of the project, which requires a considerable amount of optical power. In addition, the trap depth of the DMD-potential was improved by increasing the amount of optical power in the DMD path. The high power in both paths resulted in a thermal lens in both paths, most pronounced by the TeO_2 crystal. At this stage, the optical lattice path did not have a fibre to spatially filtered the beam. The thermal lens resulted in an aberrated beam profile for the optical lattice, and as such, a poor trap quality. For the DMD path, thermal lensing resulted in poor coupling to the fibre; while more power was coupled into the fibre, the outgoing power remained almost unchanged.

A.2.2 Background

In a paper published by Simonelli et al. [55], thermal lensing in TeO_2 crystals is investigated. Contrary to thermal lensing in most optical components, the lens induced by the TeO_2 crystal diverges the beam. To measure the focal distance of the thermally induced lens, the waist of the beam is measured and compared to the beam waist when the AOM is removed, i.e. when no thermal lensing occurs,

$$\frac{w_l}{w_0} = \frac{1}{\sqrt{1 + \left(\frac{z_R}{f_{\text{th}}}\right)^2}}, \tag{A.1}$$

with w_l and w_0 the lensing induced waist and the old waist, z_R the Rayleigh length and f_{th} the focal distance of the thermally induced lens.

As the thermally induced lens introduces a small curve in the wavefront, the focal distance of the lens, f_{th}, is large. The thermal lens is most effectively cancelled when $z_R \gg f_{\text{th}}$, i.e. when z_R is small. The waist is measured by focussing the beam on a camera after propagation through the AOM.

To cancel thermal lensing, a Galilean telescope consisting of two lenses of short focal distances, separated by $f_1 + f_2 + \delta z$, is created. The short focal distance ensures a small Rayleigh length, z_R, and the δz slightly converges or diverges the wavefront, which is then collimated again by the thermal lens due to the AOM. The distance required to focus the

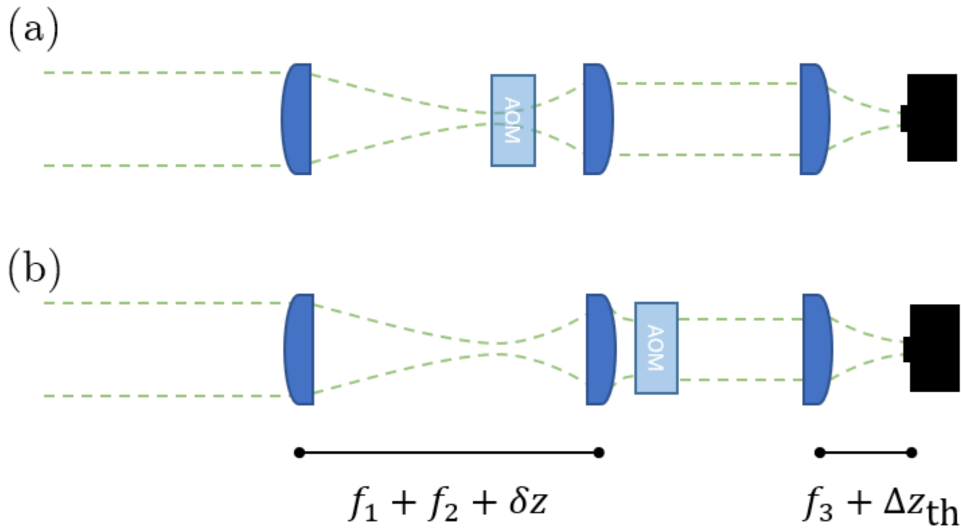

FIGURE A.3: The setup for measuring thermal lensing, with the AOM located at the point of least thermal lensing. Figure (a) depicts the situation in which the AOM is put close to the waist of the beam in the telescope. Figure (b) corresponds to the situation in which the AOM is put right after the telescope. The telescope is slightly misaligned by δz, to create a collimated wavefront when combined with the induced thermal lens of the AOM. The shift in imaging distance, Δz_{th} is zero in absence of thermal lensing.

beam on the camera is given by $f_3+\Delta z_{\text{th}}$, with Δz_{th} the induced shift due to thermal lensing. In the situation where thermal lensing is not present, $\Delta z_{\text{th}} \to 0$. When modelling the system using ABCD-matrices for Gaussian beams, $\Delta z_{\text{th}} \to 0$ at two locations: Next to the waist in the telescope, where the curve in the wavefront is small, and right after the telescope, as depicted in Fig. A.3.

A.2.3 Experimental implementation

To measure Δz_{th}, the experiment is performed with and without an AOM present in the setup. The distance between f_1 and f_2 is varied by δz and the distance from the lens f_3 and the camera is measured. To find Δz_{th}, the distance between f_3 and the camera without, and with AOM present is subtracted.

The data is compared to the data from Simonelli et al., to qualitatively compare the trend of the curve. The data is plotted in Fig. A.4. The experiment is performed for the configuration where the AOM is placed outside of the telescope (Fig. A.3(b)). While this method is less effective than placing the AOM inside the telescope, the beam waist is larger at this point, reducing the change to damage the AOM with the laser.

For the configuration of Fig. A.3(b), Δz_{th} goes through zero twice. The point of the maximum shift in Δz_{th} corresponds to the point where the telescope is aligned perfectly, which results in a large thermal lens. Two distinct difference can be observed between the literature data and the UQ experimental data: The centre of the peak is at a different location, and the amplitude of the shift is much larger in the UQ data. The difference in centre of the peak can be attributed to the authors using different lenses and beam sizes in their setup. The difference in amplitude can be attributed to use of a different wavelength laser. Simonelli et al. used a 1064 nm laser for their work, while UQ data was taken with a 532 nm laser. It is obvious that the absorption coefficient for TeO_2 is much higher in the visible range than it is for the near-infrared.

After this data is taken, the alignment in the first telescope can be set to one of the points at which Δz_{th} is close to zero. One may choose the point with the lowest derivative, to avoid a rapid increase in thermal lensing when thermal drift occurs in the system. The misalignment of the telescope, however, is much larger at this point, which results in an increased (collimated) beam size. Once the telescope is set to the right δz, the setup is free of a thermal lens, regardless of the laser power.

This method proves effective against thermal lensing. Upon implementation at UQ, the coupling efficiency to the fibre coupler in the DMD-path and – at the time implemented – fibre coupler in the optical lattice path did not exceed 50%. The low efficiency was attributed

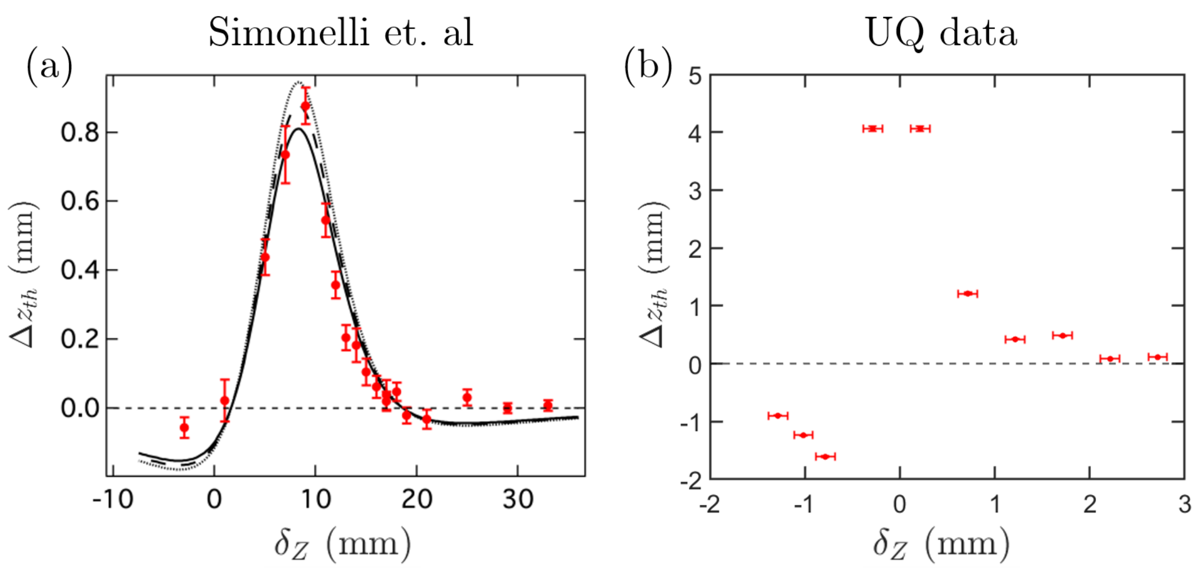

Figure A.4: The measured thermal shift as function of the 'misalignment' in the telescope δz. Panel (a) shows the experimental data and fit of Simonelli et al. Panel (b) shows the experimental data at UQ. The data from UQ follows a similar trend as the data by Simonelli. The difference in location of the peak and amplitude of z_{th} is attributed to different laser power and wavelength, which changes the absorption in the AOM crystal and the use of different lenses, which changes the location of the centre of the peak. Panel (a) adapted from "Realization of a high power optical trapping setup free from thermal lensing effects ", C Simonelli et al., *Opt. Express* **27**, 27215-27228 [55].

to the increased beam size, due to how the telescope was aligned. As the use of a fibre was required for the DMD path and desired for the optical lattice path, the TeO_2 AOMs were replaced by B-coated dense flint-glass AOMs. While the overall efficiency of these AOMs is lower, thermal lensing effects were much less pronounced. Future work in which fibre coupling is not required, but optics with a high absorption coefficient are used, could use this method for cancelling thermal lensing.

References

[1] M. H. Anderson, J. R. Ensher, M. R. Matthews, C. E. Wieman, and E. A. Cornell. *Observation of bose-einstein condensation in a dilute atomic vapor.* Science **269**(5221), 198 (1995). URL `https://science.sciencemag.org/content/269/5221/198`.

[2] K. B. Davis, M. O. Mewes, M. R. Andrews, N. J. van Druten, D. S. Durfee, D. M. Kurn, and W. Ketterle. *Bose-einstein condensation in a gas of sodium atoms.* Phys. Rev. Lett. **75**, 3969 (1995). URL `https://link.aps.org/doi/10.1103/PhysRevLett.75.3969`.

[3] G. Gauthier, I. Lenton, N. M. Parry, M. Baker, M. J. Davis, H. Rubinsztein-Dunlop, and T. W. Neely. *Direct imaging of a digital-micromirror device for configurable microscopic optical potentials.* Optica **3**(10), 1136 (2016). URL `http://www.osapublishing.org/optica/abstract.cfm?URI=optica-3-10-1136`.

[4] R. J. Rengelink, Y. van der Werf, R. P. M. J. W. Notermans, R. Jannin, K. S. E. Eikema, M. D. Hoogerland, and W. Vassen. *Precision spectroscopy of helium in a magic wavelength optical dipole trap.* Nature Physics **14**(11), 1132 (2018). URL `https://doi.org/10.1038/s41567-018-0242-5`.

[5] M. C. Beeler, R. A. Williams, K. Jiménez-García, L. J. LeBlanc, A. R. Perry, and I. B. Spielman. *The spin hall effect in a quantum gas.* Nature **498**(7453), 201 (2013). URL `https://doi.org/10.1038/nature12185`.

[6] G. Gauthier, S. S. Szigeti, M. T. Reeves, M. Baker, T. A. Bell, H. Rubinsztein-Dunlop, M. J. Davis, and T. W. Neely. *Quantitative acoustic models for superfluid circuits.* Phys. Rev. Lett. **123**, 260402 (2019). URL `https://link.aps.org/doi/10.1103/PhysRevLett.123.260402`.

[7] G. Gauthier, M. T. Reeves, X. Yu, A. S. Bradley, M. A. Baker, T. A. Bell, H. Rubinsztein-Dunlop, M. J. Davis, and T. W. Neely. *Giant vortex clusters in a two-dimensional quantum fluid.* Science **364**(6447), 1264 (2019). `https://science.sciencemag.org/content/364/6447/1264.full.pdf`, URL `https://science.sciencemag.org/content/364/6447/1264`.

[8] J. L. Ville, T. Bienaimé, R. Saint-Jalm, L. Corman, M. Aidelsburger, L. Chomaz, K. Kleinlein, D. Perconte, S. Nascimbène, J. Dalibard, and J. Beugnon. *Loading and compression of a single two-dimensional bose gas in an optical accordion.* Phys. Rev. A **95**, 013632 (2017). URL `https://link.aps.org/doi/10.1103/PhysRevA.95.013632`.

[9] A. Einstein. *Quantentheorie des einatomigen ideal gases (quantum theory of a monotamic ideal gas)*. Sitzungsberichte der Preussichen Akademie der Wissenschaften (1925). An English translation of the article can be found here https://www.thphys.uni-heidelberg.de/~amendola/otherstuff/einstein-paper-v2.pdf. A copy of the original version can be found here, URL https://www.lorentz.leidenuniv.nl/history/Einstein_archive/Einstein_1925_publication/index.html.

[10] S. N. Bose. *Plancks gesetz und lichtquantenhypothese (planck's law and the light quantum hypothesis)*. Zeitschrift für Physik (1924). The original paper by Bose was rejected. Einstein translated it into German and published it under Bose's name. An English version can be found here https://wavewatching.net/lost-papers/plancks-law-and-light-quantum-hypothesis/. A copy of the original version can be found here, URL https://tu-dresden.de/mn/physik/itp/tqo/ressourcen/dateien/lehre_dir/vorlesungen_dir/ws_2012_2013/folder-2012-12-21-5820555304/bose_1924.pdf?lang=en.

[11] D. J. Wineland, R. E. Drullinger, and F. L. Walls. *Radiation-pressure cooling of bound resonant absorbers*. Phys. Rev. Lett. **40**, 1639 (1978). URL https://link.aps.org/doi/10.1103/PhysRevLett.40.1639.

[12] D. Steck. *Rubidium 87 d line data* (2001). URL https://www.steck.us/alkalidata/rubidium87numbers.pdf.

[13] H. F. Hess. *Evaporative cooling of magnetically trapped and compressed spin-polarized hydrogen*. Phys. Rev. B **34**, 3476 (1986). URL https://link.aps.org/doi/10.1103/PhysRevB.34.3476.

[14] D. J. Griffiths and D. F. Schroeter. *Introduction to quantum mechanics* (Cambridge University Press, 2018).

[15] C. J. Pethick and H. Smith. *Bose-Einstein condensation in dilute gases* (Cambridge university press, 2008).

[16] D. Schroeder. *An Introduction to Thermal Physics*. Always learning (Pearson Education, 2013). URL https://books.google.nl/books?id=XjECngEACAAJ.

[17] A. L. Fetter and J. D. Walecka. *Quantum theory of many-particle systems* (Courier Corporation, 2012).

[18] M. T. Reeves, T. P. Billam, B. P. Anderson, and A. S. Bradley. *Identifying a superfluid reynolds number via dynamical similarity*. Phys. Rev. Lett. **114**, 155302 (2015). URL https://link.aps.org/doi/10.1103/PhysRevLett.114.155302.

[19] R. Grimm, M. Weidemüller, and Y. B. Ovchinnikov. *Optical dipole traps for neutral atoms*. Advances in Atomic, Molecular, and Optical Physics **42**, 95 (2000). URL http://www.sciencedirect.com/science/article/pii/S1049250X0860186X.

[20] D. J. Griffiths. *Introduction to electrodynamics; 4th ed.* (Pearson, Boston, MA, 2013). Re-published by Cambridge University Press in 2017.

[21] G. Gauthier. *Transport and Turbulence in Quasi-Uniform and Versatile Bose-Einstein Condensates*. Ph.D. thesis, University of Queensland (2019). URL `https://doi.org/10.14264/uql.2019.682`.

[22] W. Ketterle and N. J. Van Druten. *Evaporative cooling of trapped atoms*. Advances in Atomic, Molecular, and Optical Physics pp. 181–236 (1996). URL `http://inis.iaea.org/search/search.aspx?orig_q=RN:28065975`.

[23] E. Majorana. *Atomi orientati in campo magnetico variabile*. Il Nuovo Cimento (1924-1942) **9**(2), 43 (1932). URL `https://doi.org/10.1007/BF02960953`.

[24] D. G. Grier. *A revolution in optical manipulation*. Nature **424**(6950), 810 (2003). URL `https://doi.org/10.1038/nature01935`.

[25] M. Gajdacz, P. L. Pedersen, T. Mørch, A. J. Hilliard, J. Arlt, and J. F. Sherson. *Non-destructive faraday imaging of dynamically controlled ultracold atoms*. Review of Scientific Instruments **84**(8), 083105 (2013). `https://doi.org/10.1063/1.4818913`, URL `https://doi.org/10.1063/1.4818913`.

[26] C. C. Bradley, C. A. Sackett, and R. G. Hulet. *Bose-einstein condensation of lithium: Observation of limited condensate number*. Phys. Rev. Lett. **78**, 985 (1997). URL `https://link.aps.org/doi/10.1103/PhysRevLett.78.985`.

[27] O. Sezerman and G. Best. *Accurate alignment preserves polarization*. Laser focus world **33**(12), S27 (1997).

[28] J. Klaers, J. Schmitt, F. Vewinger, and M. Weitz. *Bose-einstein condensation of photons in an optical microcavity*. Nature **468**(7323), 545 (2010). URL `https://doi.org/10.1038/nature09567`.

[29] J. Kasprzak, M. Richard, S. Kundermann, A. Baas, P. Jeambrun, J. M. J. Keeling, F. M. Marchetti, M. H. Szymańska, R. André, J. L. Staehli, V. Savona, P. B. Littlewood, B. Deveaud, and L. S. Dang. *Bose-einstein condensation of exciton polaritons*. Nature **443**(7110), 409 (2006). URL `https://doi.org/10.1038/nature05131`.

[30] I. Humbert. *All-optical 87Rb Bose-Einstein condensate apparatus: construction and operation*. Ph.D. thesis, Univeristy of Queensland (2012).

[31] M. Egorov, B. Opanchuk, P. Drummond, B. V. Hall, P. Hannaford, and A. I. Sidorov. *Measurement of s-wave scattering lengths in a two-component bose-einstein condensate*. Phys. Rev. A **87**, 053614 (2013). URL `https://link.aps.org/doi/10.1103/PhysRevA.87.053614`.

[32] W. Wieser. *An optical dipole trap for ultracold bosons and fermions*. Master's thesis, Diplomarbeit, Ludwig-Maximilians University Munich (2006).

[33] J. W. Abraham, M. Bonitz, C. McDonald, G. Orlando, and T. Brabec. *Quantum breathing mode of trapped systems in one and two dimensions.* New Journal of Physics **16**(1), 013001 (2014). URL `https://doi.org/10.1088%2F1367-2630%2F16%2F1%2F013001`.

[34] J.-L. Ville. *Quantum gases in box potentials : sound and light in bosonic Flatland.* Theses, PSL Research University (2018). URL `https://tel.archives-ouvertes.fr/tel-01925194`.

[35] K. Husimi. *Miscellanea in Elementary Quantum Mechanics, II.* Progress of Theoretical Physics **9**(4), 381 (1953). `http://oup.prod.sis.lan/ptp/article-pdf/9/4/381/5231296/9-4-381.pdf`, URL `https://doi.org/10.1143/ptp/9.4.381`.

[36] M. E. Gehm, K. M. O'Hara, T. A. Savard, and J. E. Thomas. *Dynamics of noise-induced heating in atom traps.* Phys. Rev. A **58**, 3914 (1998). URL `https://link.aps.org/doi/10.1103/PhysRevA.58.3914`.

[37] S. Friebel, C. D'Andrea, J. Walz, M. Weitz, and T. W. Hänsch. co_2*-laser optical lattice with cold rubidium atoms.* Phys. Rev. A **57**, R20 (1998). URL `https://link.aps.org/doi/10.1103/PhysRevA.57.R20`.

[38] V. Strouhal. *Ueber eine besondere art der tonerregung.* Annalen der Physik **241**(10), 216 (1878). The original paper appeared in the German journal 'Annalen der Physik'. An English translation for the paper has never appeared., URL `https://onlinelibrary.wiley.com/doi/abs/10.1002/andp.18782411005`.

[39] L. Onsager. *Introductory talk [on liquid helium].* In *International conference of theoretical physics (Science Council of Japan, 1953)*, pp. 877–880 (1953).

[40] M. T. Reeves. *Quantum Analogues of Two-Dimenstional Classical Turbulence.* Ph.D. thesis, Univeristy of Otago (2017). URL `http://hdl.handle.net/10523/7528`.

[41] W. J. Kwon, J. H. Kim, S. W. Seo, and Y. Shin. *Observation of von kármán vortex street in an atomic superfluid gas.* Phys. Rev. Lett. **117**, 245301 (2016). URL `https://link.aps.org/doi/10.1103/PhysRevLett.117.245301`.

[42] T. Bell. *Engineering Time-Averaged Optical Potentials for Bose-Einstein Condensates.* Ph.D. thesis, Univeristy of Queensland (2019).

[43] S. W. Seo, B. Ko, J. H. Kim, and Y. Shin. *Observation of vortex-antivortex pairing in decaying 2d turbulence of a superfluid gas.* Scientific Reports **7**(1), 4587 (2017). URL `https://doi.org/10.1038/s41598-017-04122-9`.

[44] J. Allen and A. Misener. *Flow of liquid helium ii.* Nature **141**(3558), 75 (1938). URL `https://doi.org/10.1038/141075a0`.

[45] J. Allen and H. Jones. *New phenomena connected with heat flow in helium ii.* Nature **141**(3562), 243 (1938). URL `https://doi.org/10.1038/141243a0`.

[46] L. Landau. *Theory of the superfluidity of helium ii.* Phys. Rev. **60**, 356 (1941). URL `https://link.aps.org/doi/10.1103/PhysRev.60.356`.

[47] C. Manning. *Looking for the superfluid fountain effect in a bose-einstein condensate.* Honours thesis, University of Queensland (2020).

[48] D. A. Wharam, T. J. Thornton, R. Newbury, M. Pepper, H. Ahmed, J. E. F. Frost, D. G. Hasko, D. C. Peacock, D. A. Ritchie, and G. A. C. Jones. *One-dimensional transport and the quantisation of the ballistic resistance.* Journal of Physics C: Solid State Physics **21**(8), L209 (1988). URL `https://doi.org/10.1088%2F0022-3719%2F21%2F8%2F002`.

[49] B. J. van Wees, H. van Houten, C. W. J. Beenakker, J. G. Williamson, L. P. Kouwenhoven, D. van der Marel, and C. T. Foxon. *Quantized conductance of point contacts in a two-dimensional electron gas.* Phys. Rev. Lett. **60**, 848 (1988). URL `https://link.aps.org/doi/10.1103/PhysRevLett.60.848`.

[50] K. Terabe, T. Hasegawa, T. Nakayama, and M. Aono. *Quantized conductance atomic switch.* Nature **433**(7021), 47 (2005). URL `https://doi.org/10.1038/nature03190`.

[51] F. G. Aga, J. Woo, J. Song, J. Park, S. Lim, C. Sung, and H. Hwang. *Controllable quantized conductance for multilevel data storage applications using conductive bridge random access memory.* Nanotechnology **28**(11), 115707 (2017). URL `http://dx.doi.org/10.1088/1361-6528/aa5baf`.

[52] W. Wu, Z. Li, S.-Y. Wang, and P. J. Kuekes. *Method and apparatus for molecular analysis using nanoelectronic circuits* **US Patent 7 947 485 B2** (2011).

[53] D. J. Papoular, L. P. Pitaevskii, and S. Stringari. *Quantized conductance through the quantum evaporation of bosonic atoms.* Phys. Rev. A **94**, 023622 (2016). URL `https://link.aps.org/doi/10.1103/PhysRevA.94.023622`.

[54] Y. Shin, M. Saba, A. Schirotzek, T. A. Pasquini, A. E. Leanhardt, D. E. Pritchard, and W. Ketterle. *Distillation of bose-einstein condensates in a double-well potential.* Phys. Rev. Lett. **92**, 150401 (2004). URL `https://link.aps.org/doi/10.1103/PhysRevLett.92.150401`.

[55] C. Simonelli, E. Neri, A. Ciamei, I. Goti, M. Inguscio, A. Trenkwalder, and M. Zaccanti. *Realization of a high power optical trapping setup free from thermal lensing effects.* Opt. Express **27**(19), 27215 (2019). URL `http://www.opticsexpress.org/abstract.cfm?URI=oe-27-19-27215`.

[56] M. N. Polyanskiy. *Refractive index database.* URL `https://refractiveindex.info`.